NASA Contractor Report 3885

Computations of Two-Dimensional Airfoil-Vortex Interactions

Ganapathi R. Srinivasan

CONTRACT NAS2-11331
MAY 1985

NASA Contractor Report 3885

Computations of Two-Dimensional Airfoil-Vortex Interactions

Ganapathi R. Srinivasan
Flow Simulations, Inc.
Sunnyvale, California

Prepared for Aeromechanics Laboratory
USAAVSCOM Research and Technology Laboratories
and NASA Ames Research Center
under Contract NAS2-11331

National Aeronautics
and Space Administration

**Scientific and Technical
Information Branch**

1985

FOREWORD

The research reported in this document was performed for NASA, Ames Research Center and U. S. Army Aeromechanics Laboratory (AVSCOM) by Flow Simulations, Inc., Sunnyvale, California under Contract NAS2-11331. During the period of performance of this contract Drs. P. Kutler and W. J. McCroskey were the Technical Monitors.

Drs. J. L. Steger, T. H. Pulliam and P. G. Buning provided some helpful suggestions during this investigation. Also, special thanks are due to Dr. P. G. Buning for his help in displaying computed results using his three-dimensional plot package.

Results of Transonic Small Disturbance calculations were provided by Dr. W. J. McCroskey.

SUMMARY

This report presents a numerical solution procedure to calculate the interaction of a vortex with a two-dimensional airfoil in a uniform free stream and results for several test cases. A Lamb-like analytically prescribed vortex with a finite core, either fixed at one location in the flowfield or convecting with the free stream, interacts with the flowfield of an airfoil made up of NACA 0012 or NACA 64A006 profile in transonic or subsonic free stream. Both Euler and thin-layer Navier-Stokes solutions are computed using perturbation form of an implicit noniterative numerical algorithm.

Euler and thin-layer Navier-Stokes solutions are compared with the solutions from transonic small disturbance formulation (ATRAN2) and experimental results where they are available. Most of the interactions considered in this study are strong, in the sense that the vortex produced significant and nonlinear distortions of the flowfield, but relatively weak in the sense that they are within the scope of the transonic small disturbance assumptions. For such interactions, the three methods gave qualitatively similar results. For the stronger interactions considered, in the sense of exceeding the small disturbance assumptions limit, Euler and thin-layer Navier-Stokes solutions are computed.

Comparison of thin-layer Navier-Stokes solution with a test case of recent Army Aeromechanics Laboratory experiments on a two-bladed helicopter rotor shows a good agreement with the surface pressure distribution. The location of the shock wave is predicted slightly downstream of the experimental observation which implies that the time-lag effects of the free stream velocity approaching the blade may be important and should be

considered in the analyses.

In general, the results show a tremendous influence of the interacting vortex on the flowfield around the airfoil. This is particularly true when the vortex is stationary. For a convecting vortex, the most dramatic changes in the airfoil flowfield seem to occur when the vortex is within one chord of the airfoil.

TABLE OF CONTENTS

SECTION PAGE

LIST OF SYMBOLS

$\hat{A},\hat{B}$ = Jacobian matrices

a_o = vortex core radius

a_∞ = free stream sound speed

C = characteristic length scale, chord of the airfoil

C_D = drag coefficient

C_L = lift coefficient

C_{LV} = lift equivalent vortex strength $(=2\Gamma)$

C_p = coefficient of pressure

$\hat{E},\hat{E}_o$ = flux vectors

e = total energy per unit volume

$\hat{F},\hat{F}_o$ = flux vectors

H_t = total enthalpy

I = identity matrix

J = transformation Jacobian

M_∞ = free stream Mach number

Pr = Prandtl number

p = pressure

p_∞ = free stream static pressure

$\vec{Q}$ = velocity vector

$\vec{Q}_v$ = velocity induced by the vortex, $\vec{i}u_v + \vec{j}v_v$

$\vec{Q}_\infty$ = free stream velocity

$\hat{q}$ = unknown flowfield vector

$\hat{q}_o$ = Euler solution of vortex in a uniform free stream

Re = Reynolds number

r = radial distance from the vortex center
$\vec{r}_o$ = initial position of the vortex, $\vec{i}x_o + \vec{j}y_o$
r_ℓ = airfoil leading edge radius
$\hat{S}$ = viscous flux vector
U,V = contravariant velocity components
u_∞,v_∞ = free stream velocity components in x and y directions
u,v = velocity components in physical plane in x and y directions
u_v,v_v = velocity components induced by the vortex in x and y directions
v_θ = tangential velocity
x_o,y_o = initial vortex location in the flowfield
x_v,y_v = instantaneous position of the vortex
x,y,t = physical plane coordinates
α = angle of attack
β = compressibility factor, $(1 - M_\infty)^{\frac{1}{2}}$
Γ = strength of vortex ($\frac{1}{2}C_{LV}$)
γ = ratio of specific heats
$\varepsilon_E,\varepsilon_I$ = explicit and implicit smoothing coefficients
θ = the angle which the vortex velocity vector makes with y-axis
κ = coefficient of thermal conductivity
Λ = angle between vortex axis and rotor blade chord line
λ = second coefficient of viscosity
μ = coefficient of viscosity
ξ,η,τ = transformed plane coordinates
$\xi_x,\xi_y,..$ = metrics of transformation
ρ = density
ρ_∞ = free stream density

ϕ = disturbance potential

Ω = angular velocity of the rotor

Subscripts

v = refers to vortex

∞ = refers to free stream

LIST OF FIGURES

1. INTRODUCTION

The interaction of concentrated vortices with lifting surfaces is encountered in many aerodynamic and fluid dynamic applications. Although poorly understood, the interaction mechanism can have a significant influence on the aerodynamics, aeroelasticity, and aeroacoustics of maneuvering vehicles and especially so in the transonic flow regime. This is because in transonic flow the shock wave position and strength are sensitive to small changes in the flow parameters. Of particular interest, in the present study, is the interaction encountered in a helicopter rotor flowfield. The interaction of a trailing vortex wake in such a flowfield with the oncoming rotor blades can induce unsteady blade loading and aerodynamic noise. The blade tips, which trail strong and concentrated tip vortices, trace out prolate cycloidal paths in space, leading to a variety of possible blade-vortex interactions. The generic problem, shown schematically in Fig. 1, can be viewed as an unsteady, three-dimensional close encounter of a curved-line vortex, at an arbitrary intersection angle Λ, with a high aspect-ratio lifting surface that is executing combined rotational and translational motion at transonic speeds. The limiting cases of such encounter for $\Lambda = 0^o$ and 90^o are illustrated in Figs. 2a and 2b, respectively; the former encounter is essentially two-dimensional but unsteady, whereas the latter can be considered as steady but highly three-dimensional. For more discussion of these representations and their aeroacoustic implications, the reader is referred to a recent paper by George and Chang (Ref. 1).

Under certain flight conditions, helicopter rotor produces an impulsive, highly directional noise at a regular frequency corresponding to the blade passage frequency. At least two mechanisms are thought to be responsible for this impulsive noise (also called the "blade-slap"), viz, 1) shock formation on the advancing side of the blade due to local transonic flow, and 2) unsteady lift fluctuations on the blade due to interaction of the tip vortex from the preceding blade. In order to shed some light on the understanding of this second mechanism (corresponding to the case of Fig. 2a), the present study prepares groundwork for a future aeroacoustic and vibratory airloads computation capability by making unsteady two-dimensional flowfield computations of a vortex interaction with a rotorcraft airfoil.

Current numerical algorithms to compute unsteady transonic vortical flows of the helicopter rotor are frequently either inadequate or too costly to use for routine design analysis of a large class of two- and three-dimensional flowfields. Unsteady potential theory cannot be satisfactorily used for such analyses unless major assumptions are made in modeling the nonlinear vortex wake structure. Numerical algorithms based on the Euler equations are suitable for any inviscid flowfield simulation but cannot be applied to flows dominated by viscous effects, in which case the only choice is to use the Navier-Stokes equations. But current numerical algorithms for both Euler and Navier-Stokes equations used for unsteady flow computations have large computer time and storage requirements.

The motivation for the present study is two fold. The first of these is to apply a modified form of Euler and thin layer Navier-Stokes two-dimensional codes for computing the rotational compressible flowfield of the interaction of a vortex with a rotorcraft airfoil made up of either NACA 0012 or NACA 64A006 profiles. The cases of interacting vortex fixed in space in the flowfield as well as convecting past the airfoil will be considered so as to better understand the flow phenomenon and to provide benchmark solutions for checking out more approximate engineering prediction techniques. The second objective is to further the methodology of existing numerical procedures so that advanced simulations of full helicopter flowfields are possible when more powerful computers become available.

With the above objectives in mind, an implicit finite difference procedure for solving the unsteady, two-dimensional thin layer Navier-Stokes equations in conservation-law form of Steger (Ref. 2) was modified to implement the perturbation scheme of Buning and Steger (Ref. 3) to resolve non-uniform incoming streams (vortex in the present study) without having to specify far-field grid refinement. This was further modified to include the quasi-steady (vortex fixed) and unsteady (vortex convecting) vortex effects to compute the interaction flowfield in the region outside the core of the vortex. Although the concentrated vortex is analytically specified and preserved in this study, an actual experimental vortex can easily be substituted in its place. (It should be mentioned that the code has the provision to turn off viscosity and modify the boundary conditions to make Euler calculations if and when needed.) The numerical results are compared with the available experimental results (Ref. 4) and results from transonic small disturbance formulation (Refs. 5,6).

In this report the numerical formulations are discussed in Section 2. Results and discussion are presented in Section 3, and the concluding remarks are given in Section 4.

2. NUMERICAL FORMULATIONS

2.1 Governing Equations

The governing partial differential equations are the unsteady, two-dimensional, thin-layer Navier-Stokes equations (Ref. 2). These are written in non-dimensional, strong conservation-law form for a perfect gas using the generalized independent coordinate system of ξ, η, τ and in the perturbation form (Ref. 3) as

$$\partial_\tau(\hat{q} - \hat{q}_0) + \partial_\xi(\hat{E} - \hat{E}_0) + \partial_\eta(\hat{F} - \hat{F}_0) = Re^{-1}\partial_\eta\hat{S} \tag{1}$$

where

$$\hat{q} = J^{-1}\begin{bmatrix} \rho \\ \rho u \\ \rho v \\ e \end{bmatrix} \tag{2}$$

is the flowfield vector we are solving for, $\hat{q}_0$ is the solution of the Euler equations

$$\partial_\tau\hat{q}_0 + \partial_\xi\hat{E}_0 + \partial_\eta\hat{F}_0 = 0 \tag{3}$$

and, in this particular case, representes the solution of a prescribed vortex (either fixed in space or moving) in a uniform free stream. Also, the flux vectors $\hat{E}$, $\hat{F}$, and $\hat{S}$ are given by

$$\hat{E} = J^{-1}\begin{bmatrix} \rho U \\ \rho u U + \xi_x p \\ \rho v U + \xi_y p \\ (e + p)U - \xi_t p \end{bmatrix}, \quad \hat{F} = J^{-1}\begin{bmatrix} \rho V \\ \rho u V + \eta_x p \\ vV + \eta_y p \\ (e + p)V - \eta_t p \end{bmatrix} \tag{4}$$

$$\hat{S} = J^{-1}\begin{bmatrix} 0 \\ \mu(\eta_x^2 + \eta_y^2)u_\eta + (\mu/3)\eta_x(\eta_x u_\eta + \eta_y v_\eta) \\ \mu(\eta_x^2 + \eta_y^2)v_\eta + (\mu/3)\eta_y(\eta_x u_\eta + \eta_y v_\eta) \\ \kappa Pr^{-1}(\gamma - 1)^{-1}(\eta_x^2 + \eta_y^2)\partial_\eta a^2 \\ \quad + \mu(\eta_x^2 + \eta_y^2)(u^2 + v^2)_\eta/2 \\ \quad + (\mu/3)(\eta_x u + \eta_y v)(\eta_x u + \eta_y v_\eta) \end{bmatrix} \tag{5}$$

where U and V are the contravariant velocities along the ξ and η directions given by

$$\left.\begin{aligned} U &= \xi_t + \xi_x u + \xi_y v \\ V &= \eta_t + \eta_x u + \eta_y v \end{aligned}\right\} \tag{6}$$

The metrics ξ_t, ξ_x, etc., are easily formed from the derivatives of x_τ, x_ξ, etc., using the relations

$$\left.\begin{aligned} \xi_x &= Jy_\eta & \eta_x &= -Jy_\xi \\ \xi_y &= -Jx_\eta & \eta_y &= Jx_\xi \\ \xi_t &= -x_\tau\xi_x - y_\tau\xi_y & \eta_t &= -x_\tau\eta_x - y_\tau\eta_y \end{aligned}\right\} \tag{7}$$

and J is the transformation Jacobian given by

$$J = \xi_x \eta_y - \xi_y \eta_x = 1/(x_\xi y_\eta - x_\eta y_\xi) \tag{8}$$

The viscous flux vector $\hat{S}$ is written in the context of thin-layer model (Ref. 2) and hence is valid for high-Reynolds number turbulent flows. In the viscous stress terms of the flux vector $\hat{S}$, the viscosity coefficient μ is computed as the sum of $\mu_{\text{laminar}} + \mu_{\text{turbulent}}$ for turbulent boundary layer. Sutherland's equation (Ref. 7) is used to evaluate μ_{laminar}; the turbulent eddy viscosity, $\mu_{\text{turbulent}}$, is computed using a two-layer algebraic eddy viscosity model of Baldwin and Lomax (Ref. 8).

The generalized coordinate system

$$\left.\begin{aligned} \xi &= \xi(x,y,t) \\ \eta &= \eta(x,y,t) \\ \tau &= \tau \end{aligned}\right\} \tag{9}$$

allows the boundary surfaces in the physical plane to be mapped onto rectangular surfaces in the transformed plane as shown in Fig. 3. Moreover, this simplifies the procedure of grid point clustering in regions that experience rapid change in the flowfield gradients. This is particularly important in the present problem because of the presence of the interacting vortex and shock waves. Further, such a body fitted coordinate system would also simplicty the application of boundary condition procedure.

The primitive variables of Eq. (1) are the density ρ, the mass fluxes ρu, ρv in the two coordinate directions x and y and the total energy per unit volume e. In Eq. (4) the pressure p is nondimensionalized by γp_∞; density ρ by ρ_∞; velocity components u, v in x and y directions by a_∞; and the energy e by $\rho_\infty a_\infty^2$. The chord of the airfoil, C, is chosen as the reference length scale and is assumed equal to unity. The nondimensionalization also produces parameters such as Reynolds number (Re) and Prandtl number (Pr). The second coefficient of viscosity λ is assumed equal to $-2/3\mu$, after Stokes hypothesis.

The pressure, density, and velocity components are related to the energy per unit volume by the equation of state which is written for a perfect gas as

$$e = \frac{p}{\gamma - 1} + \rho\left(\frac{u^2 + v^2}{2}\right) \tag{10}$$

2.2 Boundary and Initial Conditions

Although Eq. (1) is solved for the perturbation quantity $(\hat{q} - \hat{q}_0)$, the boundary conditions are applied only to the solution variable $\hat{q}$. $\hat{q}_0$, which is the solution of Euler equations, is supposed to be known as described below.

The boundary conditions used are applied explicitly. Figure 3 shows a schematic of the solution domain. Along the outer boundary f-g-h, all the flow quantities are specified by the solution of Eq. (3) and updated at each time step. At the outflow boundaries e-f and a-h, a simple linear extra-polation is used for ρ, ρu, and ρv. The total energy e is obtained from Eq. (10) by holding the value of p equal to the free stream value (the value corresponding to the Euler solution $\hat{q}_0$). To ensure continuity across the wake cut a-b and d-e, the flow variables are linearly extrapolated from both sides of the cut and then averaged to obtain the values along the cut.

Along the body surface $\eta(x,y,t) = 0$, the no-slip condition for viscous flow without suction or injection is given by setting $V \equiv 0$ and $U \equiv 0$. The velocity components u and v are then calculated from

$$\begin{pmatrix} u \\ v \end{pmatrix} = J^{-1} \begin{bmatrix} \eta_y & -\xi_y \\ -\eta_x & \xi_x \end{bmatrix} \begin{pmatrix} -\xi_t \\ -\eta_t \end{pmatrix} \tag{11}$$

The pressure along the body surface is obtained from a normal momentum relation given by

$$P_n(\eta_x^2 + \eta_y^2)^{1/2} = J\rho(\partial_\tau \eta_t + u\ \partial_\tau \eta_x + v\ \partial_\tau \eta_y) \tag{12}$$

where n is the direction normal to the body surface. This equation is solved implicitly in ξ for pressure at the body. The density at the airfoil surface is obtained by extrapolation from the grid interior. Now since the pressure and density are known at the surface, the total energy is calculated from Eq. (10). The boundary conditions are of low order and hence require that the grid lines be clustered and normal at the body surface.

For the vortex interaction study any representation of practical vortex can be chosen. Here, a Lamb-like analytical vortex (Refs. 9,10) with a finite core is specified. The cylindrical velocity of such a vortex is given for a compressible flow by

$$\frac{v_\theta(r)}{a_\infty} = \frac{\hat{\Gamma}}{r}\left(1 - e^{-r^2/a_o^2}\right) \tag{13}$$

where v_θ is the cylindrical velocity and is a function of only the radial distance r from the vortex center, $\hat{\Gamma} = \Gamma/2\pi a_\infty C$ is the dimensionless vortex strengh, a_o is the core radius. (For most of the computations reported here a_o is assumed equal to 0.05.) For this vortex in a uniform free stream, the pressure field induced (by this vortex) is determined using the radial momentum equation

$$\frac{dp_v}{dr} = \frac{\rho_v v_\theta^2}{r} \tag{14}$$

in conjunction with the energy equation for constant enthalpy flow given by

$$\frac{\gamma}{\gamma - 1}\frac{P_v}{\rho_v} + \frac{1}{2}Q^2 = H_t \tag{15}$$

where $Q^2 = u^2 + v^2$ and H_t is the total enthalpy. Once the pressure is known, density can be determined from Eq. (15). Having known the pressure and density, the total energy e_v for the vortex flow is given by

$$e_v = \frac{P_v}{\gamma - 1} + \frac{1}{2}\rho_v Q^2 \tag{16}$$

This completes the determination of the flow vector for vortex in a uniform free stream and is given by

$$\hat{q}_0 = J^{-1} \begin{bmatrix} \rho \\ \rho u \\ \rho v \\ e \end{bmatrix}_v \qquad (17)$$

2.3 Grid Generation

Surface conforming grids, that is, grids in which one coordinate falls on the body surface, are needed to simplify the application of the body boundary condition procedure and improve the overall accuracy of the numerical scheme. The grid generation process can be divided into several tasks: a) development of accurate surface representation, b) distribution of body surface points to yield a properly clustered, smoothly varying grid, and c) generation of outer boundary and interior mesh. While several methods of grid generation techniques are currently available, (for example, elliptic solver (Ref. 11) and hyperbolic solver (Ref. 12) that is suitable for the present application, based on past experience, is an algebraic method developed at Ames Research Center. The method has been discussed in detail by Pulliam et al (Ref. 13) and is based on the original algebraic grid generation technique of Eiseman (Ref. 14); the reader is referred to Pulliam et al (Ref. 13) for details. Briefly, the airfoil coordinates are taken as input and are used to define the airfoil surface. On the surface, grid points are distributed with clustering as desired, say, for example at the nose, trailing edge, and at prescribed locations along the upper and lower surfaces of the airfoil to resolve shocks. Coarse grid solutions can be used initially to determine the locations of shock waves. The grid lines are also clustered in the normal direction at the surface to resolve the boundary layer. This grid generation scheme is quite fast and will generate a 161 x 52 grid, say, around a NACA 0012 airfoil in less than 10 sec of CPU time on a VAX 11/780.

Typical C-grids generated by this method are shown in Figs. 4 and 5a for NACA 0012 and NACA 64A006 airfoils. The grids of Figs. 4a and 4b are 161 x 52 in size and are for viscous flow computations of NACA 0012 airfoil and extend 6 chord lengths in all directions. The spacing of first node normal to the surface is 4×10^{-5}. The grid of Fig. 5a is for inviscid flow (Euler) computations of NACA 64A006 airfoil and has dimensions 181 x 45. The grid extends 10 chord lengths upstream and in y-direction and 6 chord lengths downstream of airfoil. The grid is clustered along the body surface and in the radial direction as shown in the figure. The spacing of the first node normal to the surface is 2×10^{-3} chord. The grid of Fig. 5b, shown here for comparison, is used for ATRAN2 computations of NACA 0012 airfoil. This is a 113 x 97 straight line grid extending 200 chord lengths in all directions with clustering at the leading and trailing edges as shown. The ATRAN2 grid used for the NACA 64A006 airfoil has the same spacing in the y-direction but has 186 points in the x-direction and finer clustering near the leading edge because of its small leading edge radius.

2.4 Numerical Algorithm

The numerical algorithm used to solve the conservation-law form of the thin-layer Navier-Stokes equations is based on a class of completely implicit noniterative, ADI schemes developed by Lindemuth and Killeen (Ref. 15), Briley and McDonald (Ref. 16,17), and Beam and Warming (Ref. 18,19). The procedure is a generalization of conservative, approximate factorization scheme in the "delta" form. The procedure has been successfully applied, for example, by Steger and Kutler (Ref. 20), Kutler, Chaussee, and Pulliam (Ref. 21), and Srinivasan, Chyu, and Steger (Ref. 22) for inviscid flows and by Steger (Ref. 2), Pulliam and Steger (Ref. 23), and Srinivasan, McCroskey, and Kutler (Ref. 6) for viscous flows. Use of the implicit procedure helps remove the stiffness of the problem introduced by the fine mesh.

As applied to Eq. (1) the implicit, spatially factored algorithm using Euler implicit time differencing takes the form

$$\begin{aligned}
&(I + h\,\delta_\xi \hat{A}^n - \varepsilon_I J^{-1} \nabla_\xi \Delta_\xi J) \\
&\times (I + h\,\delta_\eta \hat{B}^n + h\,\delta_\eta \hat{M}^n - \varepsilon_I J^{-1} \nabla_\eta \Delta_\eta J)(\Delta\hat{q}^n - \Delta\hat{q}_o^n) \\
&\quad = -\Delta t[\delta_\xi(\hat{E}^n - \hat{E}_o^n) + \delta_\eta(\hat{F}^n - \hat{F}_o^n) - Re^{-1}\ \delta_\eta \hat{S}^n] \\
&\qquad -\varepsilon_E J^{-1}[(\nabla_\xi \Delta_\xi)^2 + (\nabla_\eta \Delta_\eta)^2] J(\hat{q}^n - \hat{q}_o^n)
\end{aligned} \tag{18}$$

where $\hat{A}$, $\hat{B}$, and $\hat{M}$ are the Jacobian matrices $\hat{A} = \partial\hat{E}/\partial\hat{q}$, $\hat{B} = \partial\hat{F}/\partial\hat{q}$, $\hat{M} = \partial\hat{S}/\partial\hat{q}$ and I is the identity matrix. δ_ξ, δ_η are the spatial central difference operators, Δ and ∇ are forward and backward difference operators, e.g., $\Delta_\xi \hat{q} = \hat{q}(\xi + \Delta\xi, \eta) - \hat{q}(\xi, \eta)$ and for convenience $\Delta\xi = 1 = \Delta\eta$ is assumed. Indices denoting spatial location have been suppressed. The time index is denoted by h, $t = (n\ \Delta t)$ and corresponds to Euler implict time differencing where Δt corresponds to the marching step size (in time) and $\hat{q}^n = \hat{q}(n\ \Delta t)$, $\hat{q}^n = (\hat{q}^{n+1} - \hat{q}^n)$.

ε_I and ε_E are the implicit and explicit smoothing coefficients. In writing Eq. (18), it is assumed that $\hat{A}_0 \cong \hat{A}$ and $\hat{B}_0 \cong \hat{B}$ where $\hat{A}_0 = \partial\hat{E}_0/\partial\hat{q}_0$ and $\hat{B}_0 = \partial\hat{F}_0/\partial\hat{q}_0$.

Fourth-order dissipation terms such as $\varepsilon_E J^{-1}(\nabla_\xi\Delta_\xi)^2 J(\hat{q} - \hat{q}_0)$ in Eq. (18) are added explicitly and these help to control possible numerical instabilities. The addition of the implicit second order difference terms, with coefficient ε_I, operating on $(\Delta\hat{q}^n - \Delta\hat{q}_0^n)$ extends the linear stability bound of the fourth-order terms (Ref. 23).

Central differencing is used throughout the solution domain, except in regions of supersonic flow before a shock wave where upwind differencing is used. The use of upwinding for shocks is widespread in transonic potential calculations. Upwind differencing before shocks has a stabilizing effect and improves the accuracy of the calculations.

Also, the metrics of Eq. (7) are not known analytically and therefore are to be determined numerically. To accomplish this, second-order central difference formulae are used at interior points and three-point one-sided formulae are used at the boundaries.

2.5 Transonic Small Disturbance Formulation

Since the present numerical results of Euler and thin-layer Navier-Stokes equations are compared with the results from transonic small disturbance equations, it is appropriate to describe briefly the formulation of this numerical procedure. The particular version of the code used is due to McCroskey and Goorjian (Ref. 5) and is called ATRAN2 code. ATRAN2 code is a modification of Ballhaus and Goorjian's LTRAN2 code (Ref. 24) to include the high frequency term ϕ_{tt} and concentrated or distributed rotational disturbances in the flowfield.

The unsteady transonic small-disturbance equation is based on the assumption of irrotational flow, which allows the velocity field Q to be expressed in terms of a potential. The vortex is introduced as a prescribed perturbation that is itself a solution to the Euler equation. Then the equation for the disturbance potential due to the airfoil itself becomes (Ref. 5)

$$A\phi_{tt} + B\phi_{xt} = C_1\phi_{xx} + C_2(\phi_x + u_v)_x + \phi_{yy} \tag{19}$$

where

$$A = M_\infty^2$$
$$B = 2M_\infty^2$$
$$C_1 = 1 - M_\infty^2$$
$$C_2 = -\frac{1}{2}(\gamma + 1)M_\infty^2$$
$$\vec{Q} = \vec{Q}_\infty + \nabla\phi + \vec{Q}_v$$

It is important to note that Eq. (19) is nonlinear and independent solutions are not superposable, but that the velocity field can still be split into three parts: 1) the (uniform) free stream, 2) a prescribed vortical disturbance, $\vec{Q}_v$, etc., and 3) the unknown disturbance portential $\nabla\phi$.

The usual small disturbance boundary conditions are flow tangency on the body, no disturbances at $x \to -\infty$ and $y \to \pm\infty$, and $C_p = 0$ at $x \to +\infty$. The new small-disturbance boundary condition on the body $y_b = F(x,t)$ (where $y_b = F(x,t)$ defines the airfoil surface), becomes

$$\left(\frac{\partial\phi}{\partial y}\right)_{y=0} = \vec{Q}_\infty \frac{dy_b}{dx} - \vec{J}v_v \tag{20}$$

The wake behind the airfoil is represented by a branch cut through which vorticity convects at $\vec{Q}_\infty$ from the airfoil to the downstream boundary. Across this branch cut the pressure is continuous; this condition is expressed as follows:

$$(\Gamma_x + \Gamma_t)_{wake} = 0 \tag{21}$$

Equation (19) and its corresponding small-disturbance boundary conditions are solved by the Ames code ATRAN2 (Ref. 5), which uses the basic time-accurate, implicit numerical algorithm of LTRAN2 (Ref. 24). Further details of this code are described in Ref. 5.

2.6 Transonic Small-Disturbance Calculations in the Leading-Edge Region

The small-disturbance approximation has a well-known deficiency in the leading-edge region of airfoils, where neither the disturbance velocity $\Delta\phi$ nor the usual airfoil boundary condition, Eq. (20) is small enough to satisfy the basic premise of the theory (Ref. 25). The resultant loss of accuracy is often tolerable in other applications, but in the present vortex-interaction cases it poses a dilemma in interpreting the results for airfoils with small leading-edge radii. For example, NACA 64A006 airfoil, with the leading edge radius $r_\ell/C \cong 0.0025$, exhibits a rapid expansion and suction peak very near the leading edge for small angles of attack or other vertical velocity perturbations. Accordingly, the small-disturbance results presented in Refs. 1 and 5 showed strong vortex-induced leading-edge suction peaks to form and collapse rapidly on the lower surface (vortex side) of this airfoil. If real, this phenomenon would seem to be a candidate source of acoustic radiation, such as the intense impulsive noise in helicopter aeroacoustics known as "blade-slap". Therefore, special attention was given to this point in comparing the small-disturbance and Euler results.

Two important facts quickly emerged in the comparison of numerical results. First, the Euler solutions showed much smaller magnitudes of the leading-edge pressure fluctuations, as will be seen. Secondly, as reported elsewhere (Ref. 25), the small-disturbance results were found to depend upon the computational grid spacing in the leading-edge region; in the present case, upon the maximum value of dy_b/dx at the grid point nearest the leading edge and on its variation at neighboring grid points. This unsatifactory state of affairs is illustrated in Fig. 6a.

Keyfitz et al (Ref. 25) concluded that the errors in the small-disturbance results are due to the inherent approximations, and not to truncation errors. However, an improvement in the method can be obtained by introducing a simple correction in Eq. (20); namely, by replacing Q_∞ by an analytical approximation to the local velocity u near the leading edge. This is done in the spirit of a thin-airfoil blunt leading-edge correction, e.g., Van Dyke (Ref. 26), who derived a uniformly valid second-order solution for the subsonic flow near parabolic leading edges. An excellent eapproximation to Van Dyke's surface-speed distribution function Q is

$$Q(x,r_\ell,M_\infty) \cong Q_\infty \sqrt{\frac{x}{x + r_\ell/2\beta}} \qquad (22)$$

where $\beta^2 = 1 - M_\infty^2$. Equation (22) reproduces Van Dyke's theory exactly for incompressible flow. For compressible flow, Eq. (22) can be interpreted as effectively increasing the leading-edge bluntness in proportion to $1/\beta$. It may be mentioned in passing that this compressibility correction bears a superficial resemblance to the classical similarity rules of linearized thin-airfoil theory (Ref. 27). However, those rules are derived using the small-disturbance boundary condition, Eq. (20), and are therefore questionable with regard to the details of the flow in the leading-edge region for thin airfoils.

Figure 6, which is reproduced from Ref. 6, demonstrates the effect of modifying the surface-speed distribution function Q in the body boundary condition procedure near the leading edge region for thin airfoils. This treatment renders the transonic small-disturbance solutions almost, but not completely, independent of the grid spacing. It also brings them into much better agreement with the Euler solutions for the NACA 64A006 airfoil. Accordingly, the results presented in this report were obtained using this treatment.

3. RESULTS AND DISCUSSION

A two-dimensional approximation of helicopter blade-tip vortex encounter in forward flight with the following blade is obtained by simulating the interaction of a concentrated vortex with a stationary rotorcraft airfoil, as indicated in Fig. 2a. A vortex with a finite core and a Lamb-like analytical velocity distribution is considered to interact with the flowfields of NACA 0012 and NACA 64A006 airfoils. The cases of an interacting vortex fixed in space in the flowfield (quasi-steady) as well as that convecting with the flow (unsteady) are considered. Viscous as well as inviscid flowfield computations are performed. The results are compared with ATRAN2 solutions for the cases which are well within the scope of transonic small disturbance assumptions.

The numerical algorithm used for the viscous interacting flowfield is given by Eq. (18). This is a perturbed form of the standard algorithm where the disturbance or non-uniformity, $\hat{q}_0$, is supposed to be known. In the present study $\hat{q}_0$ is the solution of Euler equations that represents a vortex moving in a uniform flow. With the algorithm (Eq. 18), the boundary conditions are applied to the solution variable $\hat{q}$ instead of the perturbation quantity $(\hat{q} - \hat{q}_0)$. The advantage of this perturbation scheme is that it enables one to maintain accuracy even in the coarse-grid outer flow. Near the body, however, the grid is fine enough to resolve both the non-uniform stream $(\hat{q}_0)$ and the deviation from it $(\hat{q} - \hat{q}_0)$. This approach was first suggested and successfully used by Buning and Steger (Ref. 3) to calculate an inviscid shear flow past a cylinder.

3.1 Baseline Solutions

Baseline solutions represent the steady state solution of stationary airfoils in a uniform free stream. The airfoils considered are NACA 0012 and NACA 64A006 with a variety of flowfield conditions. For the thin-layer Navier-Stokes solution, a nominal value of Reynolds number, based on the chord of the airfoil and free stream velocity, of 6 million is used. Turbulent boundary layer flow is assumed for the entire airfoil.

The baseline Navier-Stokes solution is computed by setting $\hat{q}_0 \equiv 0$ in the algorithm, Eq. (18). In this case the numerical algorithm reduces to the standard (non-perturbed) form of Steger (Ref. 2). The baseline Euler solution is generated by turning-off viscous terms and setting $\hat{q} \equiv 0$ in Eq. (18) and in addition making suitable changes to accomodate surface boundary conditions. The steady state solution so obtained for the NACA 0012 airfoil at $\alpha = 0.5$ deg in a uniform flow of $M_\infty = 0.8$ is shown in Fig. 7 for the three methods in the form of plots of coefficients of pressure (C_p). The agreement between the Navier-Stokes and Euler solutions is good, indicating that the viscous effects are relatively small for this case. However, ATRAN2 solution predicts the lower surface shock wave to be weaker and to occur upstream of that predicted by the Navier-Stokes and Euler codes. This is due in part to the leading-edge correction which was found to be too large for this airfoil, and in part to the limitation of the small-disturbance approximation. Nevertheless, all three methods give solutions which have good qualitative agreement. Figure 8 shows a similar baseline steady state solution for NACA 64A006 airfoil in a uniform free stream of $M_\infty = 0.85$ at at $\alpha = 0$ degrees. Also shown here are the experimental results from Zwaan (Ref. 28). The agreement is very good.

3.2 Vortex Interaction Configurations

Figure 9 shows a schematic of two configurations considered in this study. In Fig. 9a, the interacting vortex is fixed at one location in the flowfield and its influence on the airfoil flowfield is computed. For the second configuration shown in Fig. 9b, two cases are considered: 1) the vortex convecting in a prescribed path a freestream velocity, 2) the vortex convecting in a force free path at local fluid velocity.

3.2.1. Interaction of a Vortex with NACA 0012 Airfoil

(a) Vortex Fixed in Space. An analytical vortex, whose center is located at a point (x_0, y_0) in the flowfield, as shown in Fig. 9a, is made to interact with the airfoil flowfield. For Lamb-like vortex with a finite core and fixed in the flowfield, the cylindrical velocity distribution is given in the small-disturbance limit for a compressible flow by

$$\frac{v_\theta(r)}{a_\infty} \cong \frac{\hat{\Gamma}}{r} \frac{\beta}{\cos^2 \theta + \beta^2 \sin \theta} (1 - e^{-r^2/a_o^2}) \tag{23}$$

The velocity field from Eq. (23) and pressure field from Eq. (14) of the vortex are introduced into the airfoil flowfield through the vector $\hat{q}_0$ in Eq. (18) and the resulting flowfield is computed. Figure 10 shows steady state pressure distributions in the form of C_p plots for this interaction computed from three methods for a vortex located at $x_0 = 0.5$, $y_0 = -1$ and of strength $\Gamma = 0.065(C_{LV} = 0.13)$. Comparison of pressure distributions of Fig. 10 with the baseline solutions, Fig. 7, shows the dramatic influence of the vortex on the airfoil flowfield. Since the vortex induces spacially varying downwash downstream and upwash upstream of its location and also positive streamwise velocity above and negative stream velocity below its location (because of the sense of its rotation, see Fig. 9), its influence on the airfoil flowfield is determined by where it is located with respect to airfoil. The shock wave on the lower surface has moved downstream with all three methods of computation, ATRAN2 showing a much larger influence than the other two methods. Evidently the small disturbance, irrotational approximation to Euler equations introduces errors in the solution.

Figure 10 also lists the coefficients of lift and drag values. Comparison of these numbers with the baseline values shows the extent of the vortex influence on the flowfield of the airfoil. For example, the lift and drag coefficients for the baseline viscous case are respectively 0.09928 and 0.001173; with the vortex interaction these values change to $C_L = 0.05757$ and $C_D = 0.01457$.

<u>(b) Vortex Convecting with the Flow</u>. So far, the results of vortex interaction with an airfoil were presented where the vortex was fixed at one location in the flowfield. In this section, the vortex is made to convect with free stream velocity $\vec{Q}_\infty$ as shown in Fig. 9b and allowed to interact with the flowfield around the airfoil. This case approximately simulates a practical flow situation on a helicopter blade in contrast to the fixed vortex case.

For a moving vortex in compressible flow, the cylindrical velocity distribution is given by Eq. (13). The velocity from this and the pressure field from Eq. (14), induced by the vortex, are introduced through the vector $\hat{q}_0$ in Eq. (18) as done for fixed vortex case before.

To compute the interaction flowfield, the vortex is initially positioned at, say, the upstream grid boundary or any suitable upstream location (x_o, y_o) of the airfoil and then made to convect with the flow at the free stream velocity and along a straight line aligned with the free stream. Typical resulting unsteady solution of such an interaction for the case of vortex of strength $\Gamma = 0.2(C_{LV} = 0.4)$ initially located at $x_o = -6.0$ and $y_o = -0.26$ is presented in the form of C_p plots in Figs. 11a and 11c at several stages of vortex passage across the airfoil. The pressure distribution (C_p) presented in Fig. 11 generally typifies the history of interaction of the airfoil flowfield as the vortex passes by. The three methods of computations used here give results which are in qualitative agreement.

Examination of the pressure distributions of Fig. 11 shows the expected initial development of the pressure difference from the baseline case to resemble the case of increasing negative angle of attack (downwash influence) as the vortex is approaching the airfoil. This influence changes to that of a positive angle of attack (upwash) as the vortex passes behind the airfoil. Although the initial influence of the approaching vortex is felt by the airfoil when the vortex is only a few chords upstream of it, its influence decays very slowly even when the vortex has passed many chords downstream of it, and the return of the flow around the airfoil to the original state is an extremely slow process. This is also evident from the plot of the variation of the lift and moment coefficients as a function of the instantaneous vortex position as shown in Fig. 12. This contrasts with incompressible behavior (results presented later) where the influence of the vortex is felt approximately equally far upstream and downstream of the airfoil. Such a behavior in incompressible flow has also been observed by Parthsarathy (Ref. 29).

Comparison of pressure distributions for vortex-fixed and -moving cases shows that the unsteadiness greatly attenuates the influence of the vortex on the flowfield around the airfoil, as shown in Fig. 13. The lift and drag coefficients for this example are $C_L = -0.06332$ and $C_D = 0.02186$ for the unsteady case and $C_L = -0.30152$ and $C_D = 0.04578$ for the quasi-steady case. The aerodynamic force coefficients for the quasi-steady case, thus, are significantly higher than the values for the unsteady case. The pressure distributions shown in Fig. 13a for the unsteady and quasi-steady (vortex fixed) case are for the same vortex location with respect to airfoil in the flowfield, viz, $x_0 = x_v = 0$ (leading edge) and $y_0 = y_v = -0.26$. The corresponding flow pictures in terms of Mach number and pressure contours are delineated in Figs. 13b - 13c. The Mach number and pressure contours show the difference in quasi-steady and unsteady flowfields of such interaction. It is interesting to note that for the quasi-steady interaction of this vortex, vortex induced separation of the boundary layer was observed on the lower surface (vortex side) of the airfoil. But no separation was observed for the unsteady interaction of the same vortex.

3.2.2 Interaction of a Vortex with NACA 64A006 Airfoil

The use of this airfoil has special significance because of the numerous numerical and experimental studies done with it. It is thinner than the NACA 0012 section and has significantly smaller leading-edge radius, so it will serve as a test case to check the applicability of the Transonic Small Disturbance equations particularly near the leading edge in the presence of vortex-induced downwash against Euler and Navier-Stokes equations which are exact.

Four test cases are computed for this airfoil interacting with a moving vortex for the following conditions:

Case 1: $M_\infty = 0.85$, $\alpha = 0^o$, $\Gamma = 0.2$,
$x_o = -9.5$, $y_o = y_v = -0.52$

Case 2: $M_\infty = 0.85$, $\alpha = 0^o$ $\Gamma = 0.2$,
$x_o = -9.5$, $y_o = y_v = -0.26$

Case 3: $M_\infty = 0.85$, $\alpha = 0^o$, $\Gamma = 0.4$,
$x_o = -9.5$, $y_o = y_v = -0.26$

Case 4: $M_\infty = 0.85$, $\alpha = 0^o$, $\Gamma = 0.2$,
$x_o = -9.5$, $y_o \quad = -0.26$

In the first three cases listed above, the interacting vortex convects in a prescribed path at a constant $y_v (= y_o)$ with free stream velocity. In Case 4, the vortex convects in a force free path (variable y_v) with the local fluid velocity.

a) Vortex Convecting in a Prescribed Path

Figures 14 - 21 summarize the results of these test cases. In all these cases, the airfoil incidence is zero and the dramatic difference in C_p distribution between the upper and lower surfaces is due solely to the vortex interaction. As before, the influence of the vortex is felt more on the lower surface of the airfoil than the upper surface, a result of nonlinear effects; linear small-disturbance calculations (Ref. 5) showed the effects of the vortex to be equal and opposite on the upper and lower surface of the airfoil.

Figure 14 shows C_p plots for the Case 1 where the vortex of strength $\Gamma = 0.2$ is initially located at $x_o = -9.5$ and $y_o = -0.52$. As seen, Euler and ATRAN2 codes predict pressure fields which are in qualitative agreement. As before, the influence of the vortex on the airfoil flowfield begins for vortex position upstream and continues even when the vortex has moved far downstream of the airfoil. However, the most rapid and dramatic changes occur when the vortex is between one chord length upstream of the leading edge of the airfoil and the trailing edge. From the C_p plots presented in Fig. 14 for the vortex location at the leading edge and downstream of this, it can be seen that both Euler and ATRAN2 solutions show large similarities at all x-stations; even the shock waves on upper and lower surfaces are quite sharp for the two solutions. Figure 15 shows lift and pitching-moment variations for the airfoil as the vortex gets convected across as a function of the instantaneous vortex position. Note that both C_L and C_M are initially zero and change continuously as the vortex moves across it.

Figures 16 and 17 show a similar comparison of C_p plots for Case 2 where the vortex of strength $\Gamma = 0.2$ was initially located at the same x-location of $x_o = -9.5$ but closer to the airfoil at $y_o = -0.26$ to produce a stronger interaction. For this particular set of conditions, the interaction is quite severe in terms of the small disturbance approximation. The ATRAN2 numerical solution seems to be marginally stable, for these flow conditions, depending on the fineness of the grid geometry and on the size of the time step Δt.

The instantaneous pressure distributions on the airfoil are shown for this case at eight x-stations of vortex position in Figs. 16a - 16b for the thin-layer Navier-Stokes and Euler methods of computations and are compared with the ATRAN2 solution shown in Fig. 16c. The baseline pressure distribution for each of the methods is shown at the first x_v station of $x_v = -9.5$, where the vortex is initialized. As before, the dramatic changes occur when the vortex is within one chord from the airfoil leading edge. Before the modification of the surface boundary condition in the leading edge region, the ATRAN2 code predicted a rapid development of a sharp suction peak followed by a rapid compression-like wave in the leading edge region. However, with the modified boundary condition the magnitude of the peak was dramatically reduced as pointed out in Section 2.6. With this modification for ATRAN2 code, all the three methods predict results which are in good qualitative agreement. Even the gross aerodynamic quantities are in very good agreement for the three methods as seen in Fig. 17 where the lift and pitching moment coefficients are shown as a function of the instantaneous vortex position for this interaction.

Figure 18 shows a similar type of pressure distribution plots as Fig. 16 but for Case 3 where the vortex is located initially at the same (x_0,y_0) location as Case 2 but doubled in its strength. The rest of the conditions are identical to that of Case 2. No ATRAN2 results were obtained for this case as these conditions are quite severe and exceed the limits of small-disturbance approximation.

Instantaneous pressure distributions are presented for this case in Fig. 18 for the interaction history from thin-layer Navier-Stokes and Euler computations at eight x-stations of vortex location. As before, the trend of events is similar to that shown in Figs. 14 and 16. The sharp suction peak of the pressure distributions at the leading edge, mentioned before, is the most noteworthy event occurring for the vortex location within one chord from the airfoil leading edge (e.g., $x = -0.5$). It appears that as the interaction gets stronger, by either increased vortex strength or by closer encounter of the vortex, not only does the size of the suction peak increases but occurs earlier, i.e., even when the approaching vortex is well upstream of the leading edge of the airfoil. Using the transonic small disturbance code without leading edge correction for the surface boundary condition, both George and Chang (Ref. 1) and McCroskey and Goorjian (Ref. 5) in independent investigations have observed this kind of leading edge behavior even for weaker vortex strengths, such as Cases 1 and 2, and they concluded that this is possibly responsible for a "blade-slap"-like acoustic wave propagation. In contrast, as shown by the results presented here, the thin-layer Navier-Stokes and Euler codes predict this kind of leading edge effect only for stronger interactions.

Figure 19 shows the lift and pitching-moment coefficient plots as a function of vortex location for this interaction. As mentioned earlier, this interaction is quite strong and produced thickening of the wall boundary layer in the vicinity of shock wave. This is an early warning for eventual flow separation.

The description of the flowfield during the unsteady interaction process is delineated in Figs. 20 - 22 in the form of Mach number and pressure contour plots. The effect of doubling the vortex strength is shown in Figs. 20 - 21. Figures 20a and 20b show contour plots for Case 2 ($\Gamma = 0.2$) when the vortex location is one chord upstream of the leading edge of the airfoil. Figures 21a and 21b are for Case 3 ($\Gamma = 0.4$) and at the same instantaneous vortex location. The initial shock wave position and its movement due to doubling the vortex strength are apparent from these plots. Figures 22a and 22b are for Case 3 ($\Gamma = 0.4$) when the vortex is at $x_v = 0.2$ (right below the airfoil). Comparison of these figures with Figs. 21a and 21b shows a tremendous movement of the lower surface shock wave and modification of the leading edge flow as the vortex passes by. The Mach contour upper limit is fixed at 1.2 in these plots and this enables visualizing the progressive decrease of lower surface pressure on the airfoil as is evident from the corresponding increase of the local Mach number of the flowfield.

b) Vortex Convecting in a Force Free Path

Here the interacting vortex is convected in a force free path. As before, the vortex is initialized at an upstream location and made to convect with the flow. By doing so, not only does the vortex convect at the local fluid velocity but preferably follows a streak line. Figure 23a presents plots of instantaneous surface pressure distribution for such an interaction (Case 4) computed from Euler method. ATRAN2 results for the same cases are presented in Fig. 23b for comparison. The two methods predict qualitatively similar pressure distributions at least until the vortex reaches the trailing edge of the airfoil. From there on downstream of the airfoil, ATRAN2 results are in disagreement even qualitatively with the Euler results. It is not surprising since the transonic small disturbance formulation prescribes a wake unlike the Euler and thin-layer Navier-Stokes methods where the wake is captured and is a part of the overall solution process. This disparity in the prediction techniques is also apparent in the plots of lift, pitching moment coefficients and the y_v-travel of the vortex as shown in Fig. 24. A comparison of Figs. 16 - 17 with Figs. 23 - 24 gives an idea of the effective change in the flowfields when the vortex is simply let free to move instead of forcing it to move in a prescribed path.

3.3 Vortex Interaction in Subcritical and Subsonic Flow

This Section presents results of computations of thin-layer Navier-Stokes Code for subcritical and subsonic free stream conditions of NACA 0012 airfoil. Two free stream conditions of $M_\infty = 0.714$, $\alpha = 0$ deg., and $M_\infty = 0.3$, $\alpha = 0$ deg. are considered. The condition of $M_\infty = 0.714$ corresponds to a case where some experimental results are available to validate the present computational procedure.

Figures 25 - 26 show plots of instantaneous surface pressure distributions at different x-locations of the vortex computed from thin-layer Navier-Stokes code. These are compared with the results from a recent Army Aeromechanics Laboratory experiment of Caradonna et al (Ref. 4). The experiments were done on a two-bladed helicopter rotor.

The computations did not include any time lag effects of the blade flows, that is, the time-dependent "free stream" velocity approaching the blade, nor any three-dimensional effects. Considering this, the agreement between computations and experiment is good. The experiments indicate the position of the shock wave to be upstream of that predicted by the computations. This suggests that the time-lag effects may be important and should be considered in the analysis. But for the comparisons shown here, the agreement between experiment and computations for the vortex side of the airfoil surface (lower surface in the Figures) is very good except for the location of the shock wave, considering the difficulty of making measurements in the unsteady flows. The reason for not so good agreement on the non-vortex side of the airfoil surface is not clear at present. It should be mentioned here that the experimental rotor model had pressure taps on only one side and the model was simply inverted to get the pressure field measurements on the second surface in an almost identical second experiment. Another point to consider is that, for the free stream Mach number of $M_\infty = 0.714$, the flow is completely subcritical in the absence of a vortex. Therefore, the shock wave formation arises from the influence of the interacting vortex field.

Figures 27a - 27b show pressure distributions from thin-layer Navier-Stokes and Euler codes for various x-locations of vortex and for purely subsonic flow conditions of $M_\infty = 0.3$ and $\alpha = 0$ degrees. The other flow parameters are delineated in the figures. In general, Euler and Navier-Stokes solutions give qualitatively similar pressure distributions.

The pressure distributions at this subsonic conditions compared to transonic conditions of Fig. 11, show as before that the significant influence of vortex occurs when the approaching vortex is within on chord of the leading edge of the airfoil and its influence starts fading away even before the vortex reaches the trailing edge and the history does not persist long unlike in a transonic flow. By the time the vortex has moved 3 - 4 chords downstream of the trailing edge, the flowfield on the airfoil looks like it has reverted back to a no-vortex situation. This is apparent from the time-history plots of C_p distribution in Figs. 27a - 27b.

3.4 Preservation of Vortex by Perturbation Scheme

One of the important features of this vortex interaction problem is to resolve and preserve the vortex as it gets convected in the flowfield. Earlier studies (Ref. 10) dealing with such flows were not efficient as the convecting vortex got smeared-off in the coarse grid regions and by the time the vortex actually reached the airfoil, its peak pressure and velocity distribution was totally destroyed. To demonstrate this deficiency, Euler calculations were made using both the previous non-perturbation appraoch as well as the present perturbation approach. The results are shown in Figs. 28 - 29 in the form of plots of vortex induced lift coefficient as a function of instantaneous vortex position as the vortex moves across the airfoil. All the flow conditions are identical for the two methods including the grid geometries.

As seen in Fig. 28, as the grid gets finer, the solution accuracy improves for the non-perturbation approach. In contrast, the present perturbation approach demonstrates in Fig. 29 that it is possible to resolve and preserve the vortex even with a coarse grid.

4. CONCLUDING REMARKS

A perturbation form of an implicit numerical algorithm for thin-layer Navier-Stokes and Euler equations was used to compute two-dimensional interaction of vortex with airfoil in transonic and subsonic flows. The NACA 0012 and NACA 64A006 profiles were selected for the airfoil shape. The interacting vortex, having a Lamb-like velocity distribution, was introduced as a perturbation of the mean flow into the governing equations. The equations were then solved for the interacting flowfield. The required computational grids were generated by an algebraic grid generation scheme. The thin-layer Navier-Stokes and Euler solutions are compared with solution from ATRAN2 code and some experimental results where available.

Most of the interactions considered in this paper are strong, in the sense that the vortex produced significant and nonlinear distortions of the flowfield, but relatively weak in the sense that they are within the scope of the transonic small disturbance assumptions. For such cases, whether the vortex was stationary or moving, the three computational methods gave qualitatively similar results. The close agreement of the thin-layer Navier-Stokes and Euler results indicates that viscous effects are negligible for these interactions. In general, ATRAN2 results are in good agreement with the results from the other two methods, although needing a special leading edge treatment for thin airfoils; without this treatment, ATRAN2 results overpredicted the interaction effects in the leading edge region. In this sense, previous studies (Refs. 1,5) of such interactions using the transonic small disturbance method are in error.

For the stronger interactions considered in this paper, strong in the sense of exceeding the small disturbance limit, the Euler and Navier-Stokes solutions showed a sharp suction peak in the pressure distributions in the leading edge region followed by a rapid compression-like wave when the interacting vortex was approximately within one chord upstream of the leading edge of the NACA 64A006 airfoil.

Comparison of thin-layer Navier-Stokes solutions with the experimental results of a two-bladed helicopter rotor shows good agreement, but it suggests that the time-lag effects of the free stream velocity approaching the blade are important and should be considered in order to interpret the experimental data properly. In subsonic incompressible flows, the interacting vortex influence dies out faster compared to transonic flow conditions as the vortex passes behind the airfoil.

In all the cases considered here, the results show a tremendous influence of the vortex on the flowfield around the airfoil. This is particularly true when the vortex is stationary. For a convecting vortex, the most dramatic changes in the airfoil flowfield seem to occur when the vortex is within one chord of the airfoil.

Typical run times for these computational methods on the NASA Ames Research Center CRAY X-MP Computer, expressed as CPU time per time step per grid node, were as follows: thin-layer Navier-Stokes = 2.1×10^{-4} sec, Euler = 1.8×10^{-4} sec, and Transonic Small Disturbance = 1.0×10^{-5} sec. Thus the small disturbance code runs approximately 20 times faster than the Euler and thin-layer Navier-Stokes codes. However, the latter were found to be more accurate and robust with important consequences for the stronger interaction cases considered here.

REFERENCES

1. George, A. R. and Chang, S. B., "Noise Due to Transonic Blade-Vortex Interactions," American Helicopter Society Paper A-83-39-50-D000, May 1983.

2. Steger, J. L., "Implicit Finite-Difference Simulation of Flow About Arbitrary Two-Dimensional Geometries," AIAA Journal, Vol. 16, No. 7, July 1978, pp. 679-686.

3. Buning, P. G. and Steger, J. L., "Solution of the Two-Dimensional Euler Equations with Generalized Coordinate Transformation Using Flux Vector Splitting," AIAA Paper 82-0971, AIAA/ASME 3rd Joint Thermophysics, Fluids, Plasma and Heat Transfer Conference, June 1982, St. Louis, Missouri.

4. Caradonna, F. X., Laub, G. H., and Tung, C., "An Experimental Investigation of the Parallel Blade-Vortex Interaction", paper No. 4, Tenth European Rotorcraft Forum, August 1984, The Hague, Netherlands.

5. McCroskey, W. J. and Goorjian, P. M., "Interactions of Airfoils with Gusts and Concentrated Vortices in Unsteady Transonic Flow," AIAA Paper 83-1691, AIAA 16th Fluid and Plasma Dynamics Conference, July 1983, Danvers, Massachusetts.

6. Srinivasan, G. R., McCroskey, W. J., and Kutler, P., "Numerical Simulation of the Interaction of a Vortex with Stationary Airfoil in Transonic Flow, AIAA Paper 84-0254, AIAA 22nd Aerospace Sciences Meeting, January 1984, Reno, Nevada.

7. "Equations, Tables, and Charts for Compressible Flow," NACA Report 1135 Ames Research Staff, 1941.

8. Baldwin, B. S. and Lomax, H., "Thin Layer Approximation and Algebraic Model for Separated Turbulent Flows," AIAA Paper 78-257, AIAA 16th Aerospace Sciences Meeting, January 1978, Huntsville, Alabama.

9. Lamb, H., Hydrodynamics, 6th ed., Dover, New York, p. 592.

10. Srinivasan, G. R. and Steger, J. L., "Computation of Wing-Vortex Interaction in Transonic Flow Using Implicit Finite Difference Algorithm," NASA CR-166251, March 1981.

11. Sorenson, R. L., "A Computer Program to Generate Two-Dimensional Grids About Airfoils and Other Shapes by the Use of Poisson's Equation," NASA TM-81198, May 1980.

12. Steger, J. L. and Chaussee, D. S., "Generation of Body-Fitted Coordinates Using Hyperbolic Partial Differential Equations," SIAM J. Sci. Stat. Comput., Vol. 1, No. 4, Dec. 1980, pp. 431-437.

13. Pulliam, T. H., Jespersen, D. C., and Childs, R. E., "An Enhanced Version of an Implicit Code for the Euler Equations," AIAA Paper 83-0344,

AIAA 21st Aerospace Sciences Meeting, January 1983, Reno, Nevada.

14. Eiseman, P. R. "Geometric Methods in Computational Fluid Dynamics," ICASE Report No. 80-11, April 1980.

15. Lindemuth, I., and Killeen, I., "Alternating Direction Implicit Techniques for Two-Dimensional Magnetohydrodynamics Calculations," J. of Comp. Physics, Vol. 13, 1973, pp. 181-208.

16. Briley, W. F. and McDonald, H., "An Implicit Numerical Method for the Multi-Dimensional Compressible Navier-Stokes Equations," Report No. 911363-6, United Aircraft Research Laboratories, 1973.

17. Briley, W. R. and McDonald, H., "Solution of the Three-Dimensional Compressible Navier-Stokes Equations by an Implicit Technique," Lecture Notes in Physics, No. 35, Proceedings of the Fourth International Conference on Numerical Methods in Fluid Dynamics, ed., R. D. Richtmyer, Boulder, Colorado, June 1974, pp. 105-110.

18. Beam, R. M. and Warming, R. F., "An Implicit Finite-Difference Algorithm for Hyperbolic Systems in Conservation-Law Form," J. of Comp. Physics, Vol. 22, Sept. 1976, pp. 87-109.

19. Beam, R. and Warming, R. F., "An Implicit Factored Scheme for the Compressible Navier-Stokes Equations," AIAA Paper 77-645, June 1977, Albuquerque, New Mexico.

20. Steger, J. L. and Kutler, P., "Implicit Finite-Difference Procedures for the Computation of Vortex Wakes," AIAA Journal, Vol. 15, No. 4, April 1977, pp. 581-590.

21. Kutler, P., Chaussee, D., and Pulliam, T., "Supersonic Flow Over Ablated Nosetips Using an Implicit Unsteady Euler Equation Solver," Paper presented at the Open Forum Session of the AIAA 10th Fluid and Plasma Dynamics Conference, June 1977, Albuquerque, New Mexico.

22. Srinivasan, G. R., Chyu, W. J., and Steger, J. L., "Computation of Simple Three-Dimensional Wing Vortex Interaction in Transonic Flow," AIAA Paper 81-1206, AIAA 14th Fluid and Plasma Dynamics Conference, June 1981, Palo Alto, California.

23. Pulliam, T. H. and Steger, J. L., "On Implicit Finite-Difference Simulations of Three-Dimensional Flow," AIAA Journal. Vol. 18, No. 2, February 1980, pp. 159-167.

24. Ballhaus, W. F. and Goorjian, P. M., "Implicit Finite-Difference Computations of Unsteady Transonic Flows about Airfoils," AIAA Journal, Vol. 15, No. 12, December 1977, pp. 1728-1735.

25. Kefits, B. L., Melnik, R. E., and Grossman, B., "An Analysis of the Leading-Edge Singularity in Transonic Small-Disturbance Theory," Quarterly Journal of Mechanics and Applied Mathematics, Vol. XXXI, Part 3, May 1978, pp. 137-155.

26. Van Dyke, M. D., "Second-Order Subsonic Airfoil Theory Including Edge Effects," NACA Report 1274, 1956.

27. Shapiro, A. H., The Dynamics and Thermodynamics of Compressible Fluid Flow, Vol. I, 1953, Roland Press, New York, pp. 315-326.

28. Zwaan, R. J., "NACA 64A006 Oscillating Flap", in Compendium of Unsteady Aerodynamic Measurements, AGARD Report No. 702.

29. Parthasarathy, R., "Aerodynamic Sound Generation Due to Vortex-Airfoil Interaction," Ph.D. Dissertation, Stanford University, September 1972.

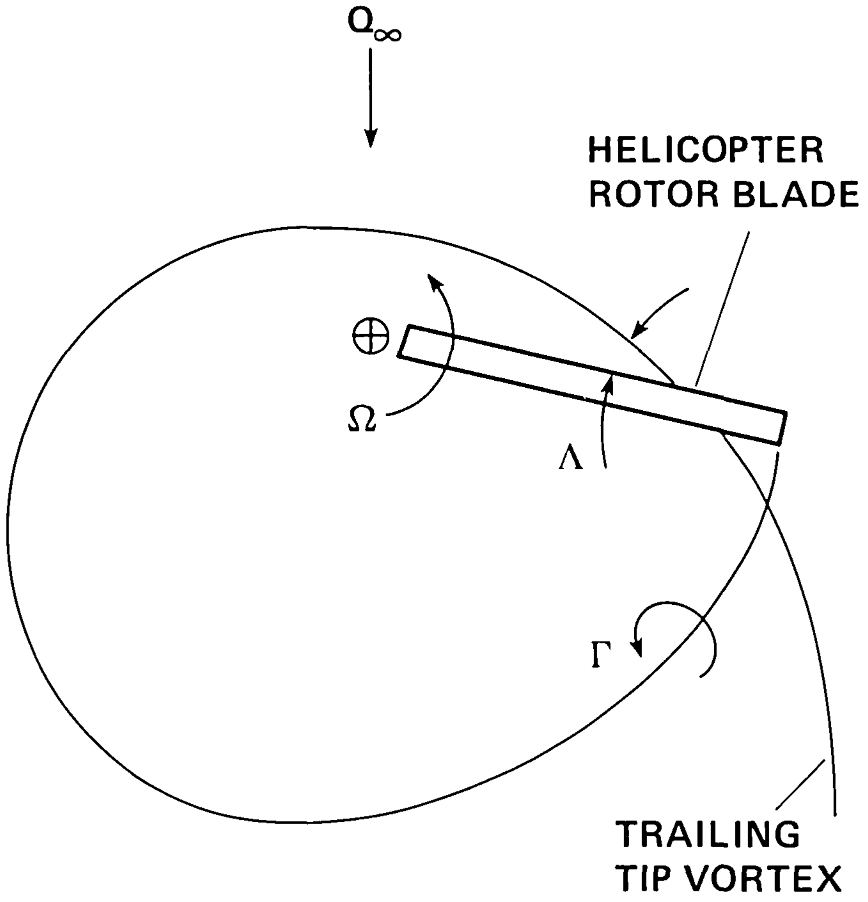

Figure 1 . Schematic of helicopter rotor-blade/vortex interaction.

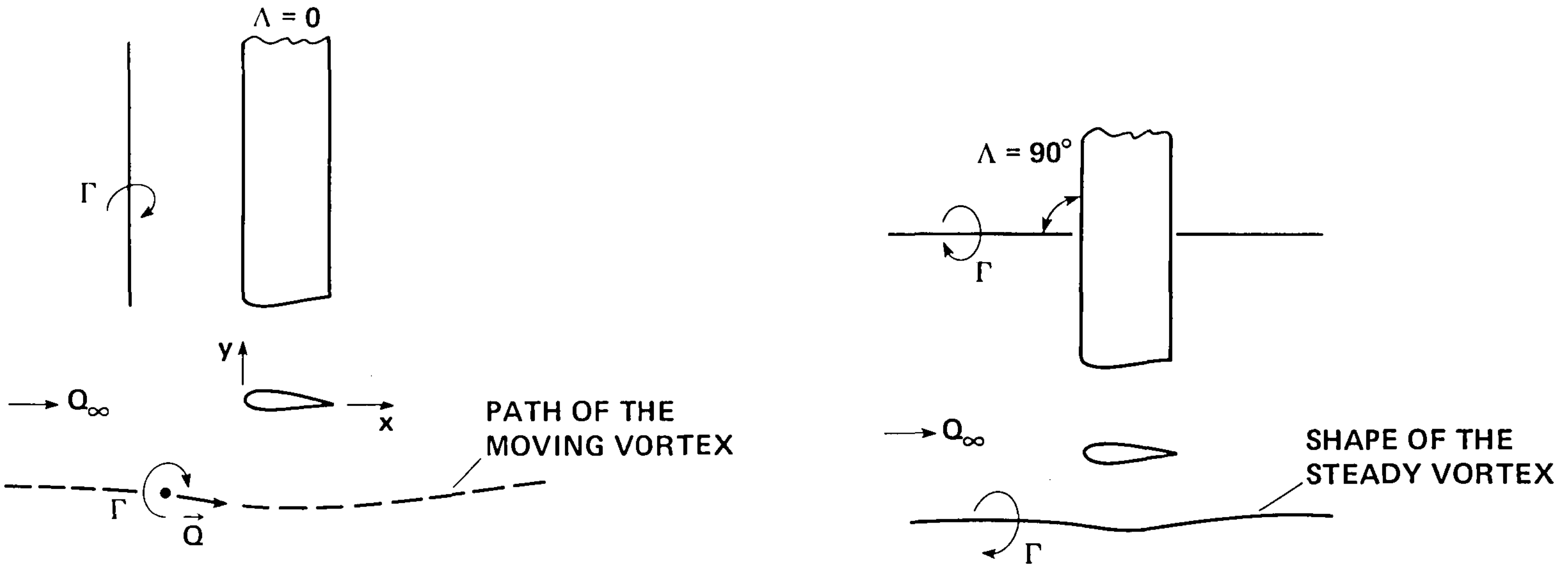

(a) VORTEX PARALLEL TO LEADING EDGE

(b) VORTEX PARALLEL TO FREE STREAM

Figure 2. Limiting cases of blade-vortex interaction problem.

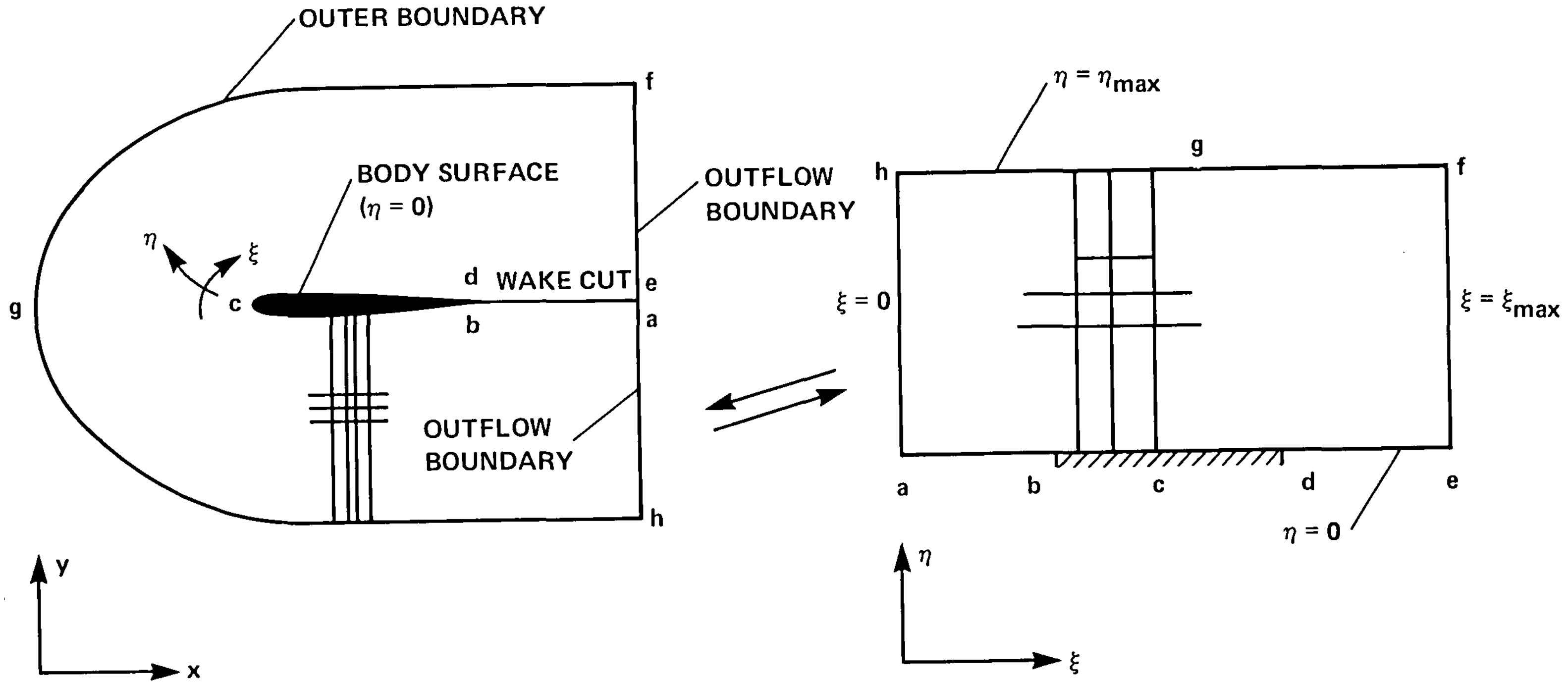

Figure 3 . Physical and computational planes.

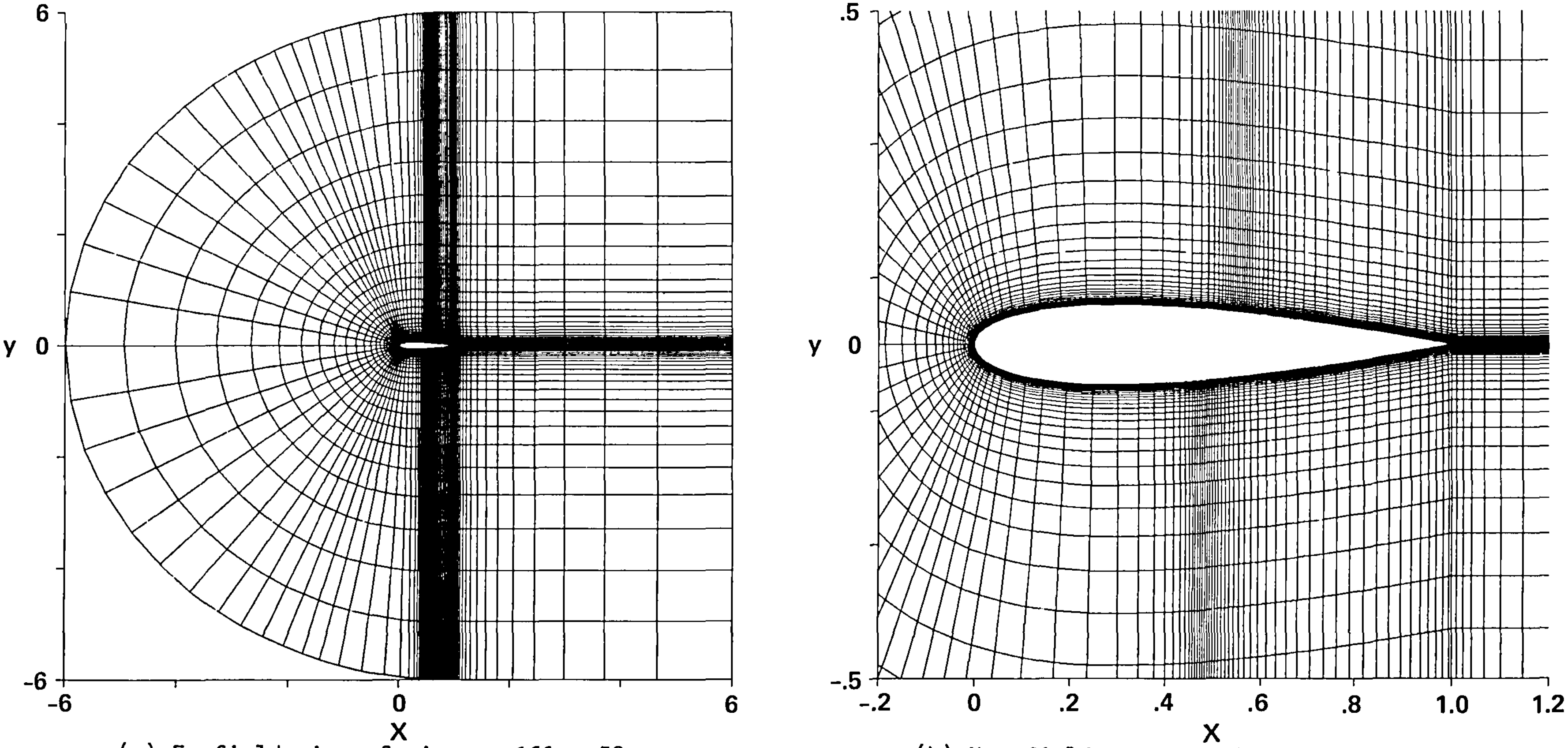

(a) Farfield view of viscous 161 x 52 C-grid for NACA 0012 airfoil.

(b) Nearfield view of viscous 161 x 52 C-grid for NACA 0012 airfoil.

Figure 4. Typical computational grids for viscous flowfield calculations.

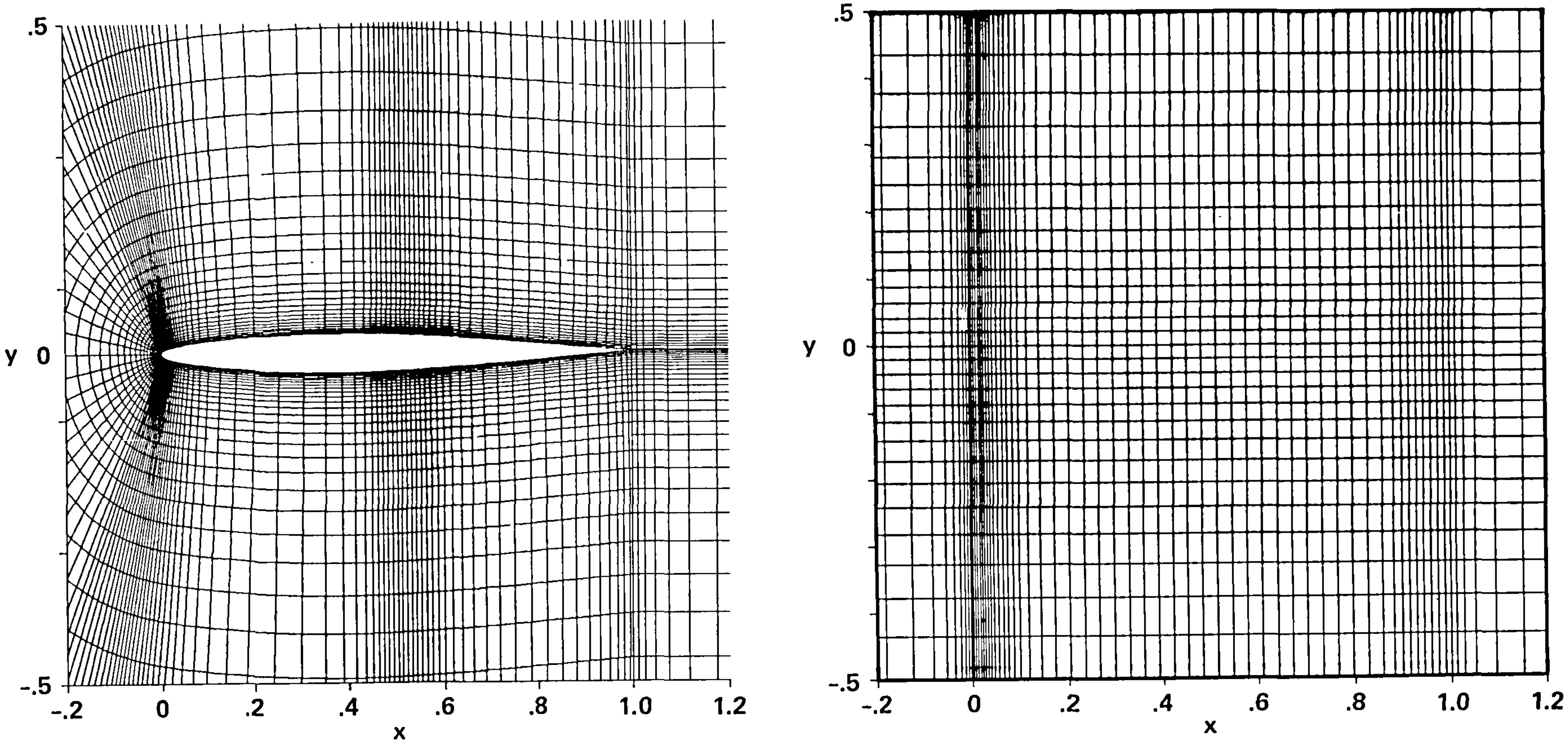

(a) Nearfield view of Euler 181 x 45 C-grid for NACA 64A006 airfoil.

(b) Nearfield view of ATRAN2 126 x 97 square grid for NACA 64A006 airfoil.

Figure 5. Typical computational grids for inviscid flowfield calculations.

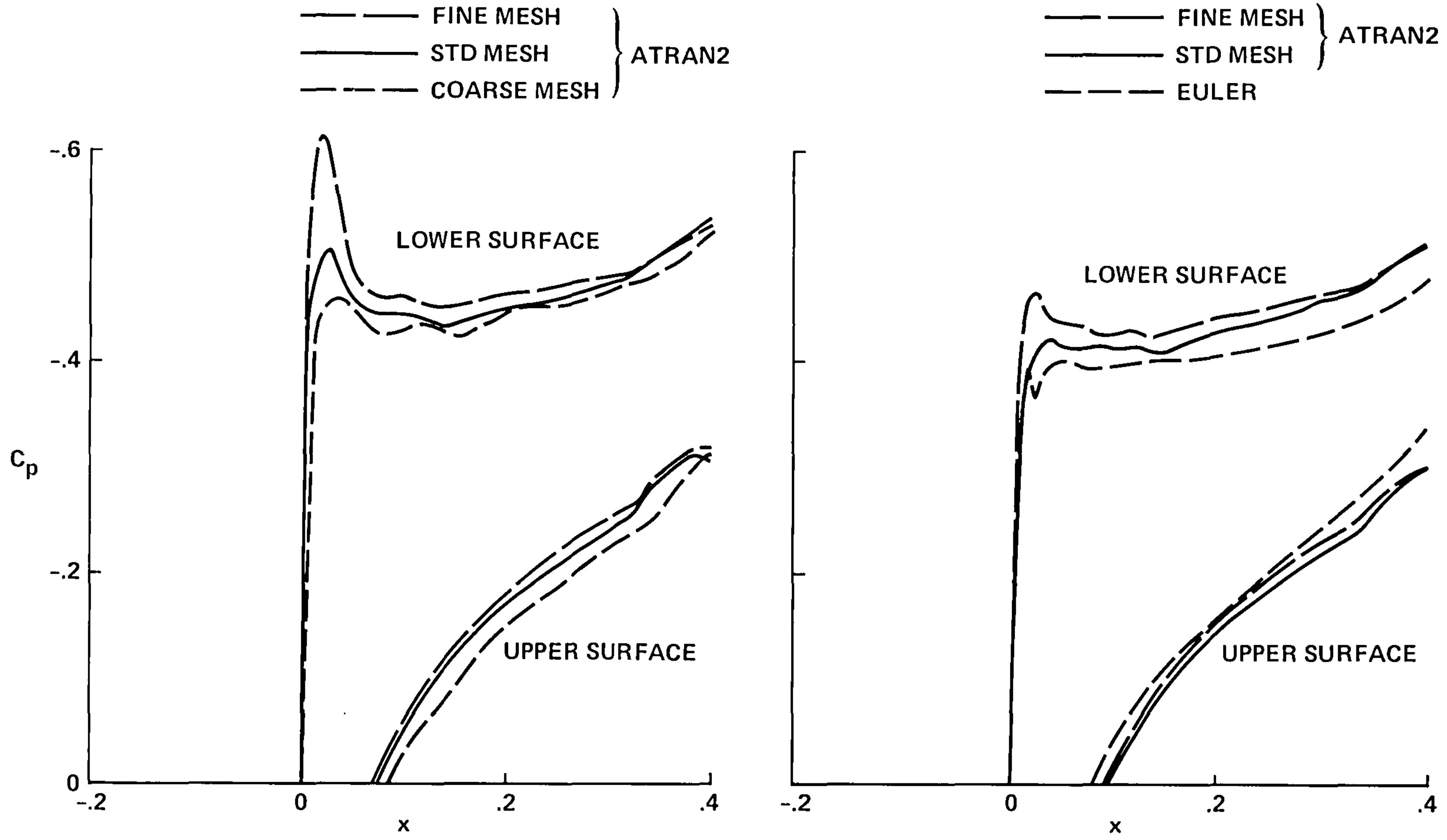

(a) without modification

(b) with modification

Figure 6. Pressure distributions in the leading edge region for the NACA 64A006 airfoil with and without leading edge modification in ATRAN2 code: $M_\infty = 0.85$, $\alpha = 0$ deg., $\Gamma = 0.2(C_{LV} = 0.4)$, $x_v = -0.3$, $y_v = 0.26$. Between $x = -0.05$ to 0 and $x = 0$ to 0.05 and at $y = 0$, the grids have the following number of grid points: coarse mesh has 5 + 9; standard mesh has 8 + 9; fine mesh has 8 + 25; while the Euler grid has 31 points between $x = 0$ and 0.05.

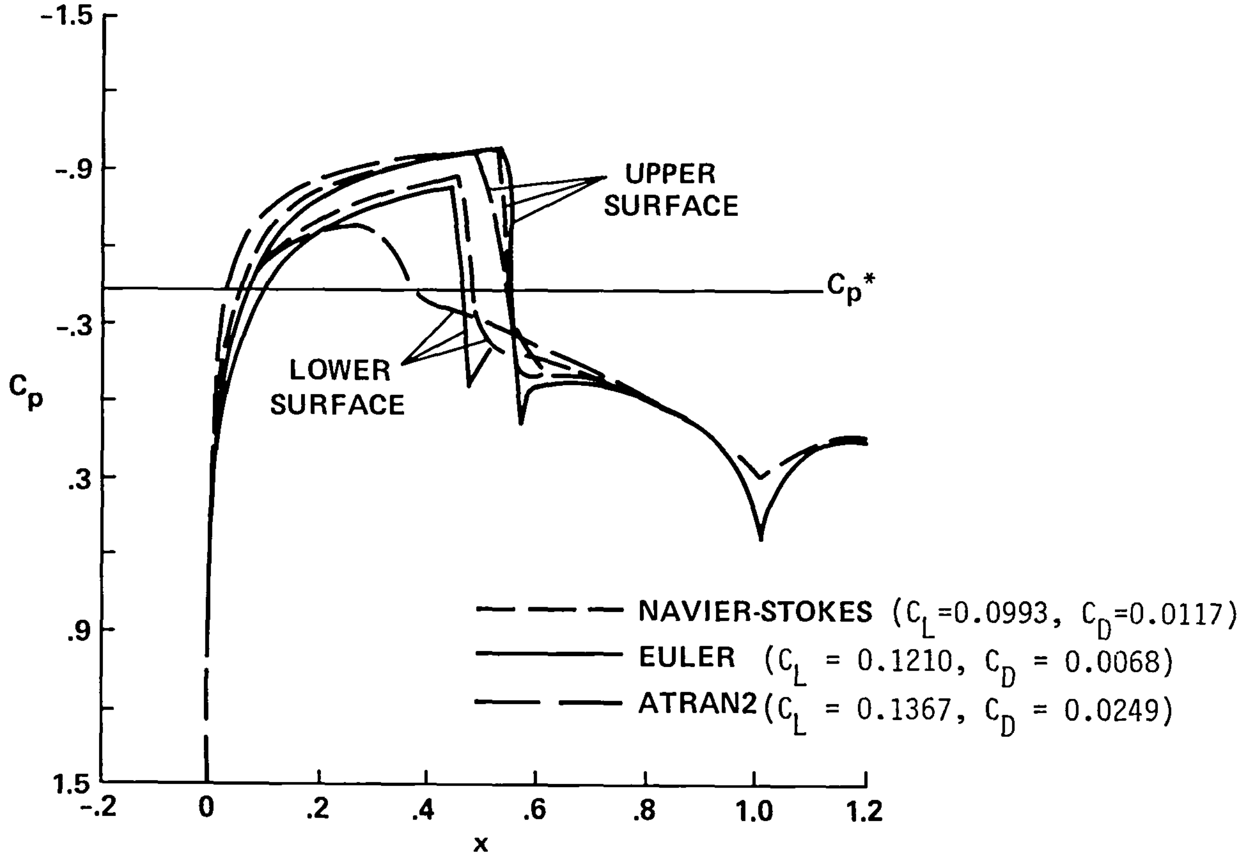

Figure 7 . Baseline pressure distribution for NACA 0012 airfoil: $M_\infty = 0.8$, $\alpha = 0.5$ deg., Re = 5.78 mil/ft.

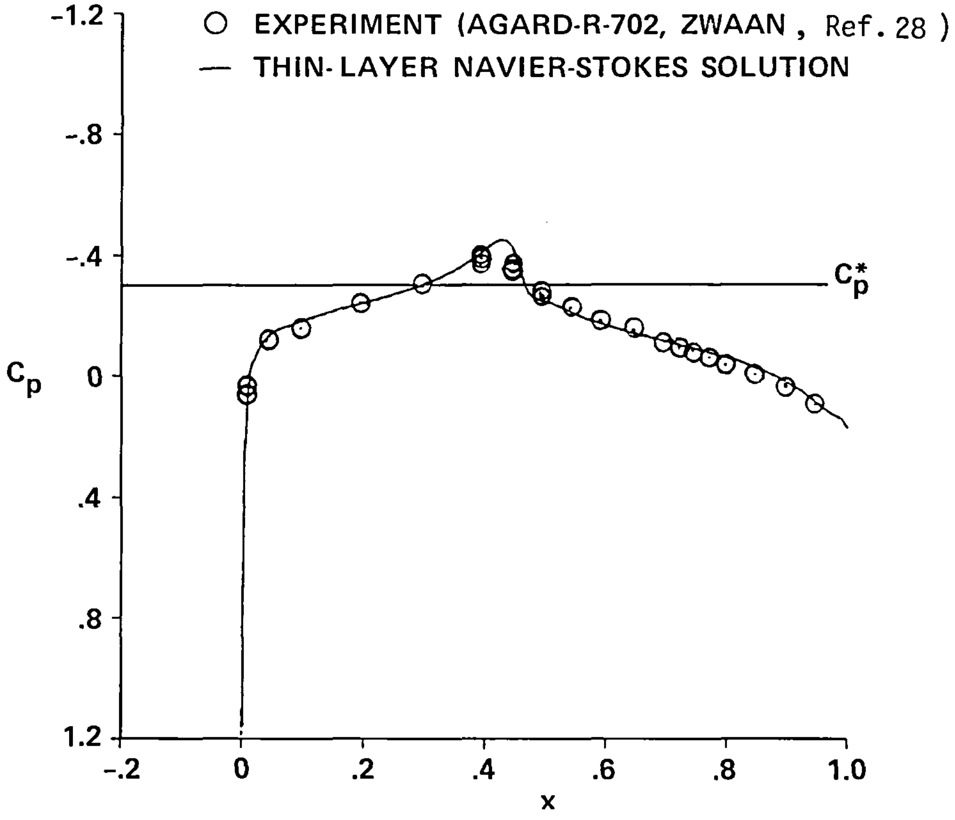

Figure 8 . Baseline pressure distribution for NACA 64A006 airfoil: $M_\infty = 0.85$, $\alpha = 0$ deg., Reynolds number of computation = 6.02 million and that of experiment = 2.28 million.

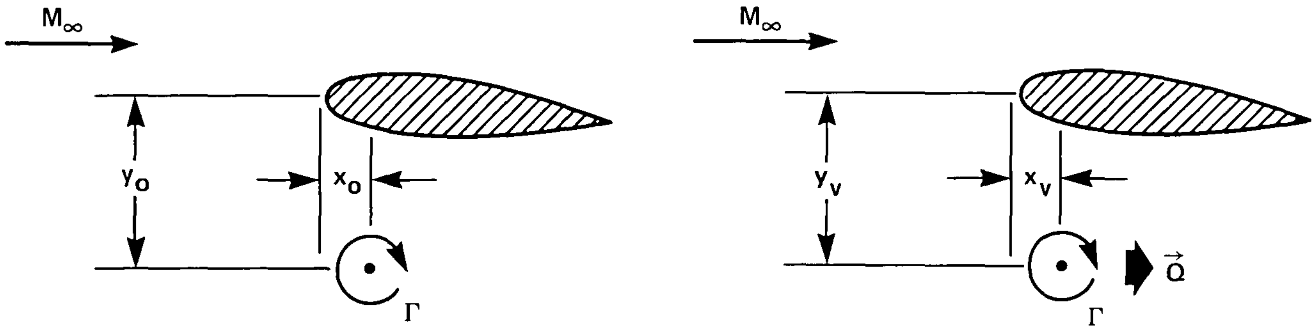

(a) VORTEX FIXED (QUASI-STEADY)

(b) VORTEX CONVECTING (UNSTEADY)

Figure 9 . Schematic of the vortex interaction configurations considered.

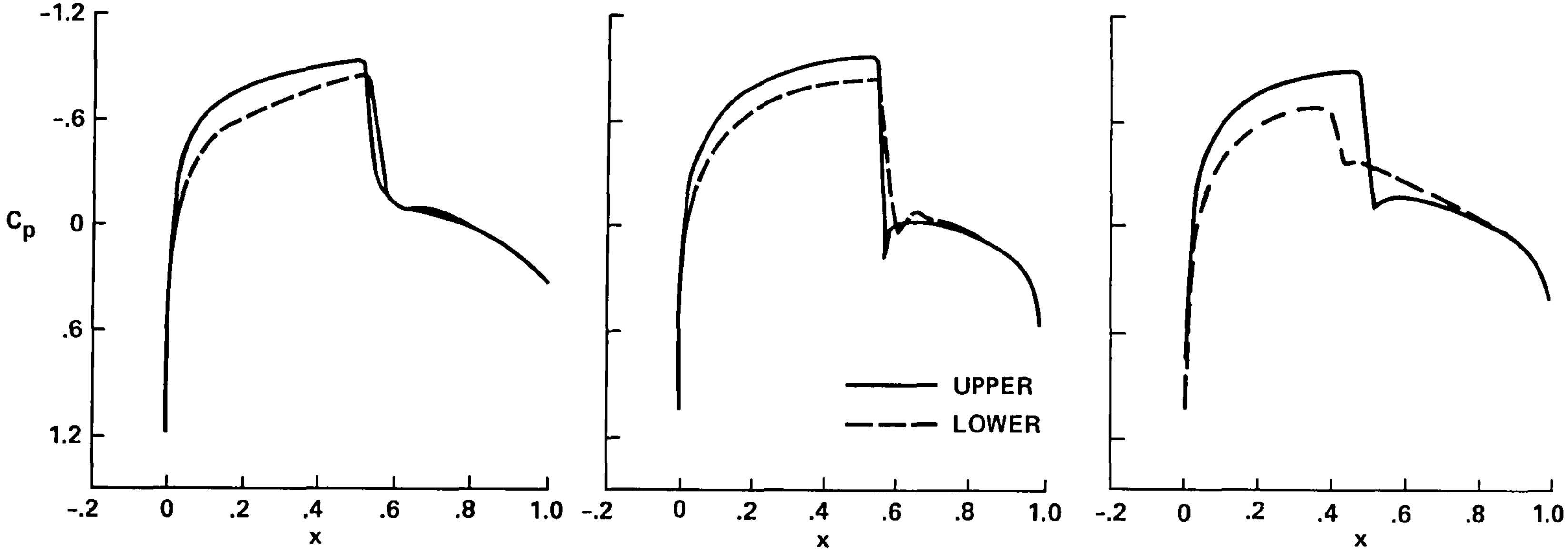

(a) THIN-LAYER NAVIER-STOKES

$C_L = 0.0576$, $C_D = 0.0146$

(b) EULER

$C_L = 0.0604$, $C_D = 0.0118$

(c) ATRAN2

$C_L = 0.1000$, $C_D = 0.0192$

Figure 10 . Quasi-steady pressure distributions of the interaction of a fixed vortex with NACA 0012 airfoil: $M_\infty = 0.8$, $\alpha = 0.5$ deg., Re = 5.78 mil/ft., $\Gamma = 0.065$ ($C_{LV} = 0.13$), $x_o = 0.5$, $y_o = -1$.

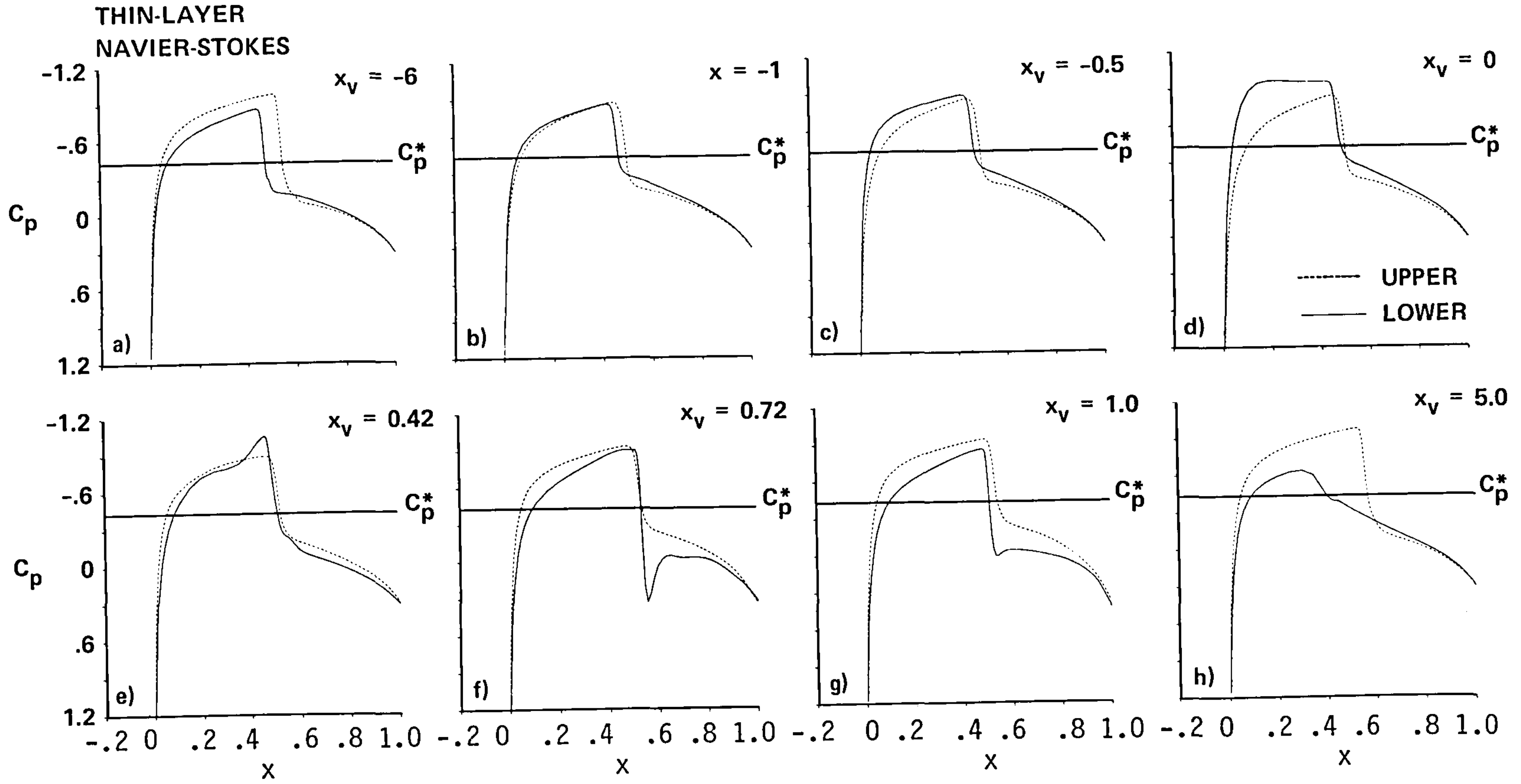

Figure 11a. Instantaneous pressure distributions during an airfoil-vortex unsteady interaction: Thin-layer Navier-Stokes solution, NACA 0012 airfoil, $M_\infty = 0.8$, $\alpha = 0.5$ deg., Re = 5.78 mil/ft., $\Gamma = 0.2$ ($C_{LV} = 0.4$), $x_o = -6.0$, $y_o = -0.26$ and $y_v = y_o - (x_v - x_o)\tan \alpha$.

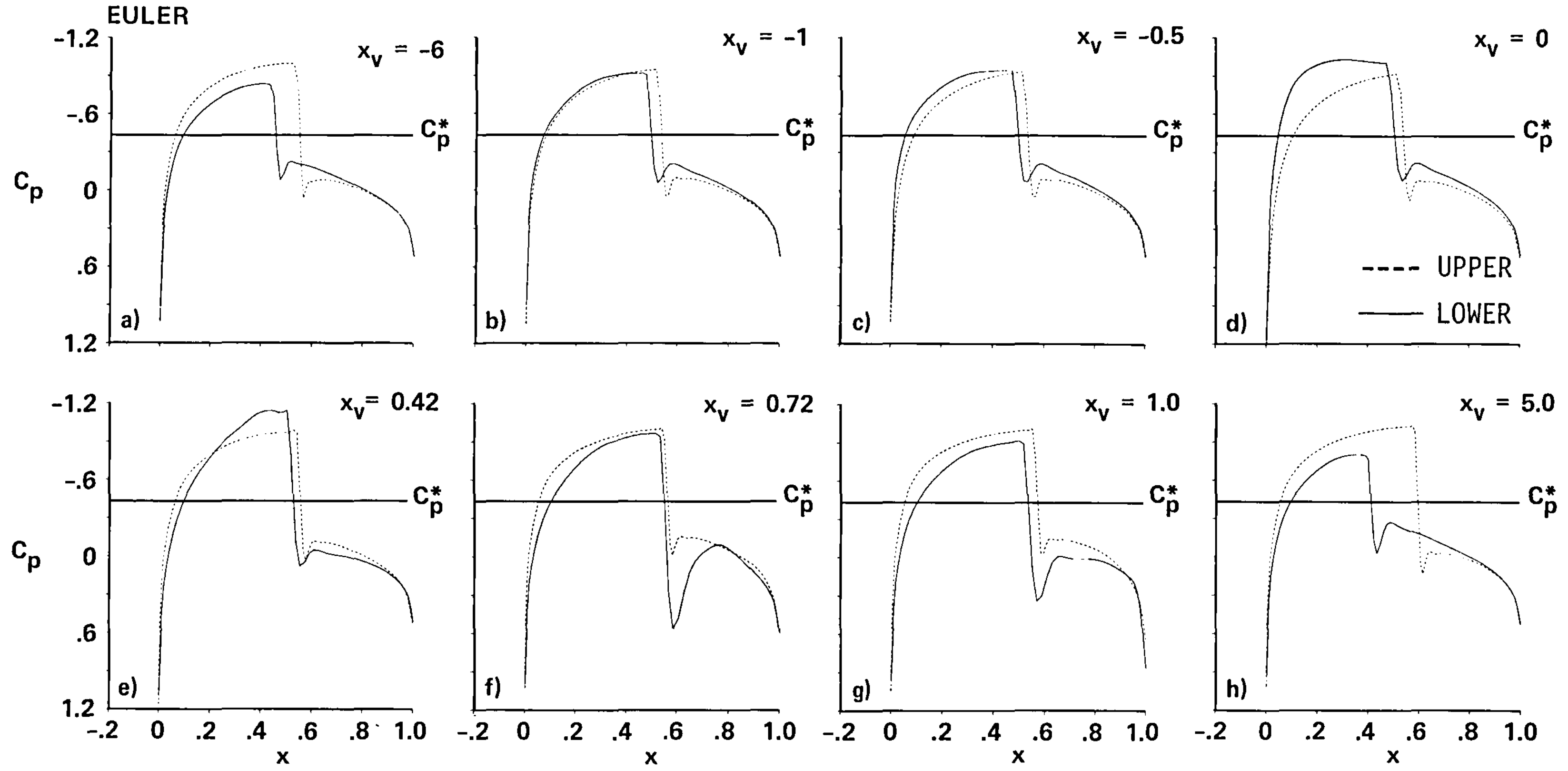

Figure 11b. Instantaneous pressure distributions during an airfoil-vortex unsteady interaction: Euler solution, NACA 0012 airfoil, $M_\infty = 0.8$, $\alpha = 0.5$ deg., Re = 5.78 mil/ft., $\Gamma = 0.2$ ($C_{LV} = 0.4$), $x_o = -6.0$, $y_o = -0.26$ and $y_v = y_o - (x_v - x_o)\tan \alpha$.

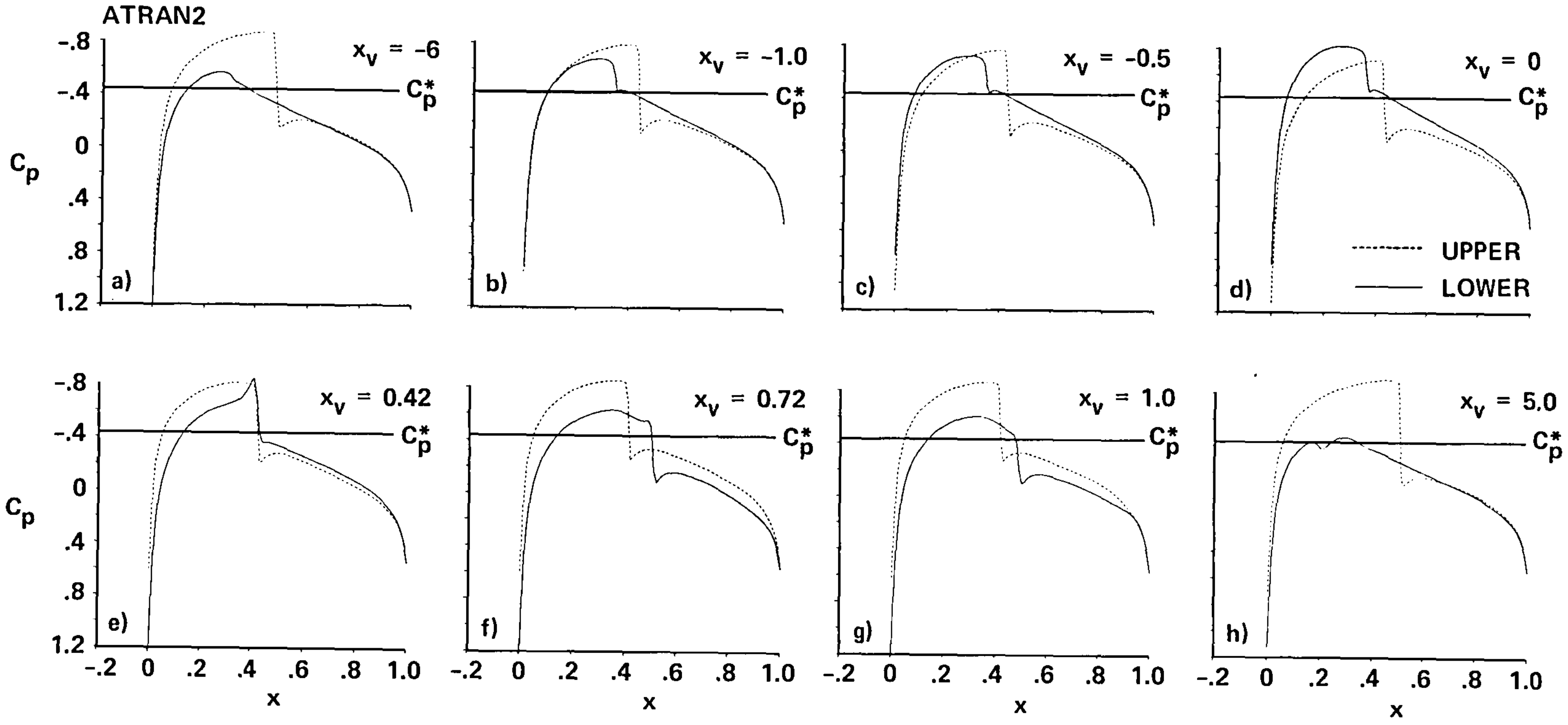

Figure 11c. Instantaneous pressure distributions during an airfoil-vortex unsteady interaction: ATRAN2 solution, NACA 0012 airfoil, $M_\infty = 0.8$, $\alpha = 0.5$ deg., Re = 5.78 mil/ft., $\Gamma = 0.2$ ($C_{LV} = 0.4$), $x_o = -6.0$, $y_o = -0.26$ and $y_v = y_o - (x_v - x_o)\tan\alpha$.

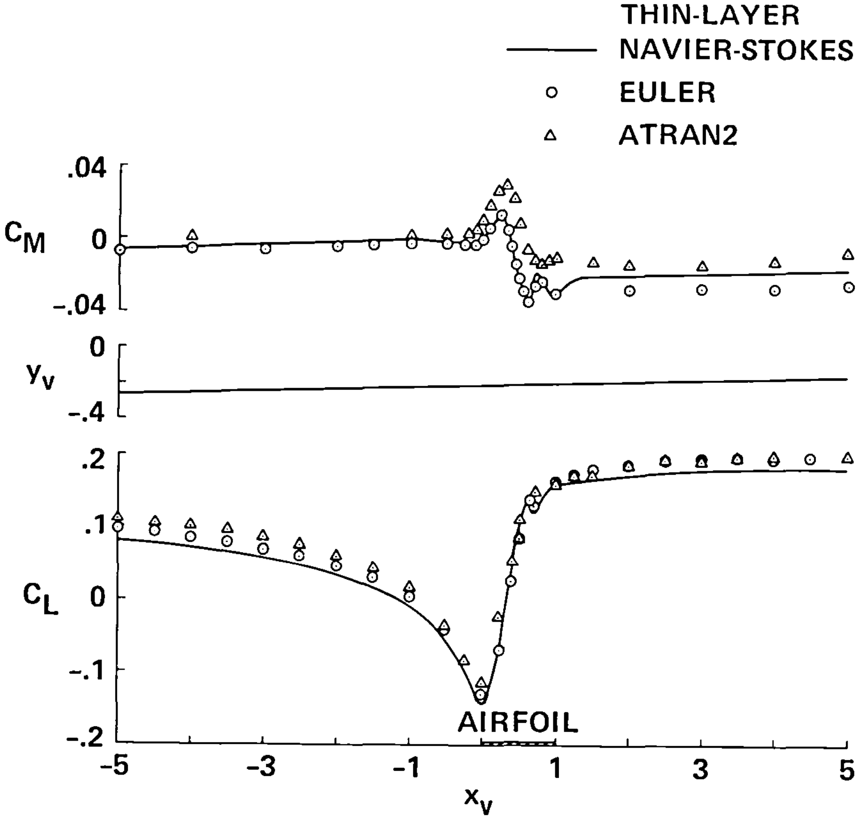

Figure 12 . Lift and pitching-moment variations with instantaneous x-position of the vortex for the conditions of Fig. 11.

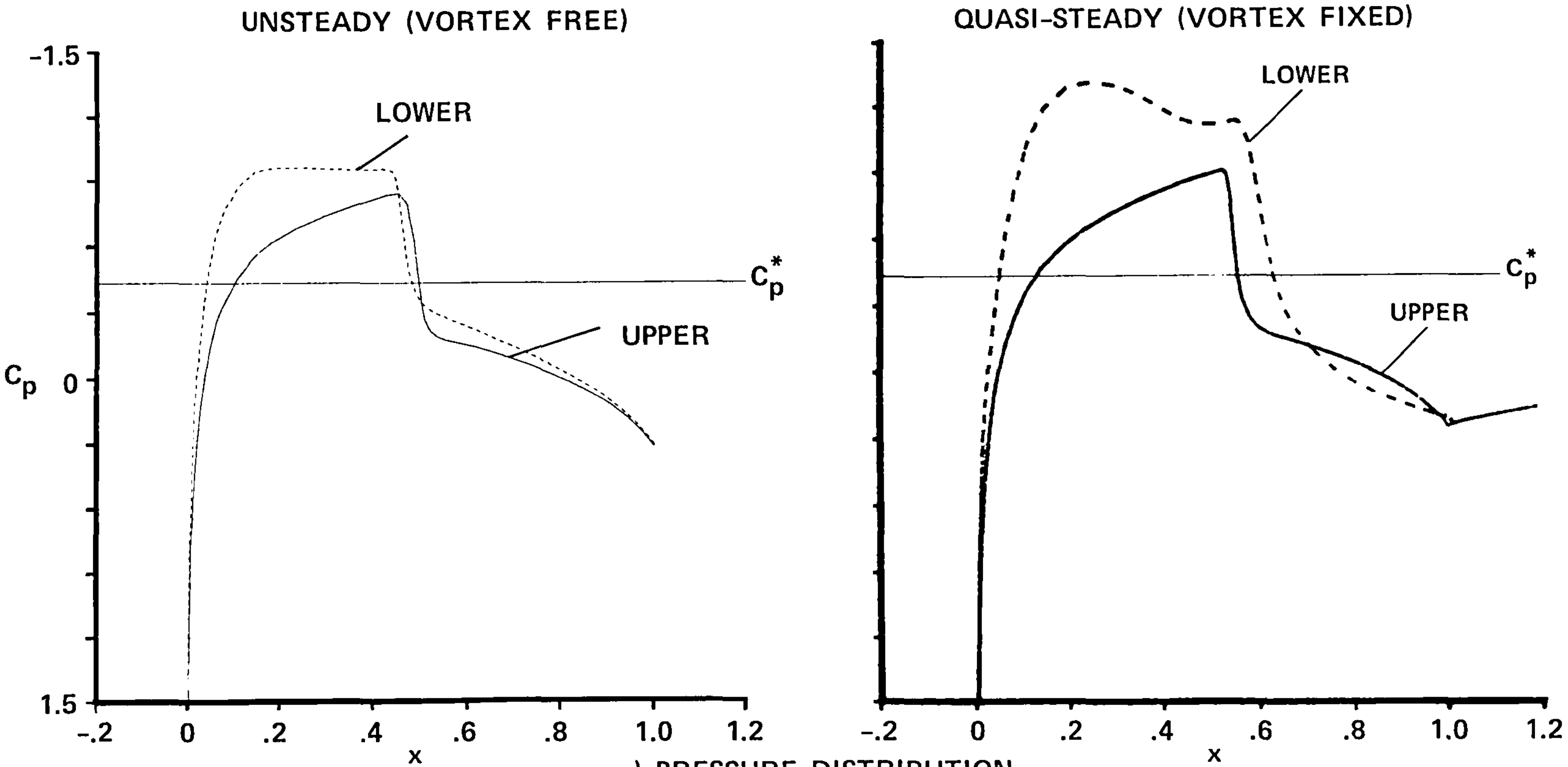

a) PRESSURE DISTRIBUTION

Figure 13 . Comparison of the unsteady and quasi-steady thin-layer Navier-Stokes solutions of the vortex-airfoil interaction: NACA 0012 airfoil, $M_\infty = 0.8$, $\alpha = 0.5$ deg., Re = 5.78 mil/ft., $\Gamma = 0.2$, for unsteady case $x_v = 0$, $y_v = 0.26$, for quasi-steady case $x_0 = 0$, $y_0 = -0.26$.

Figure 13 continued on next two pages.

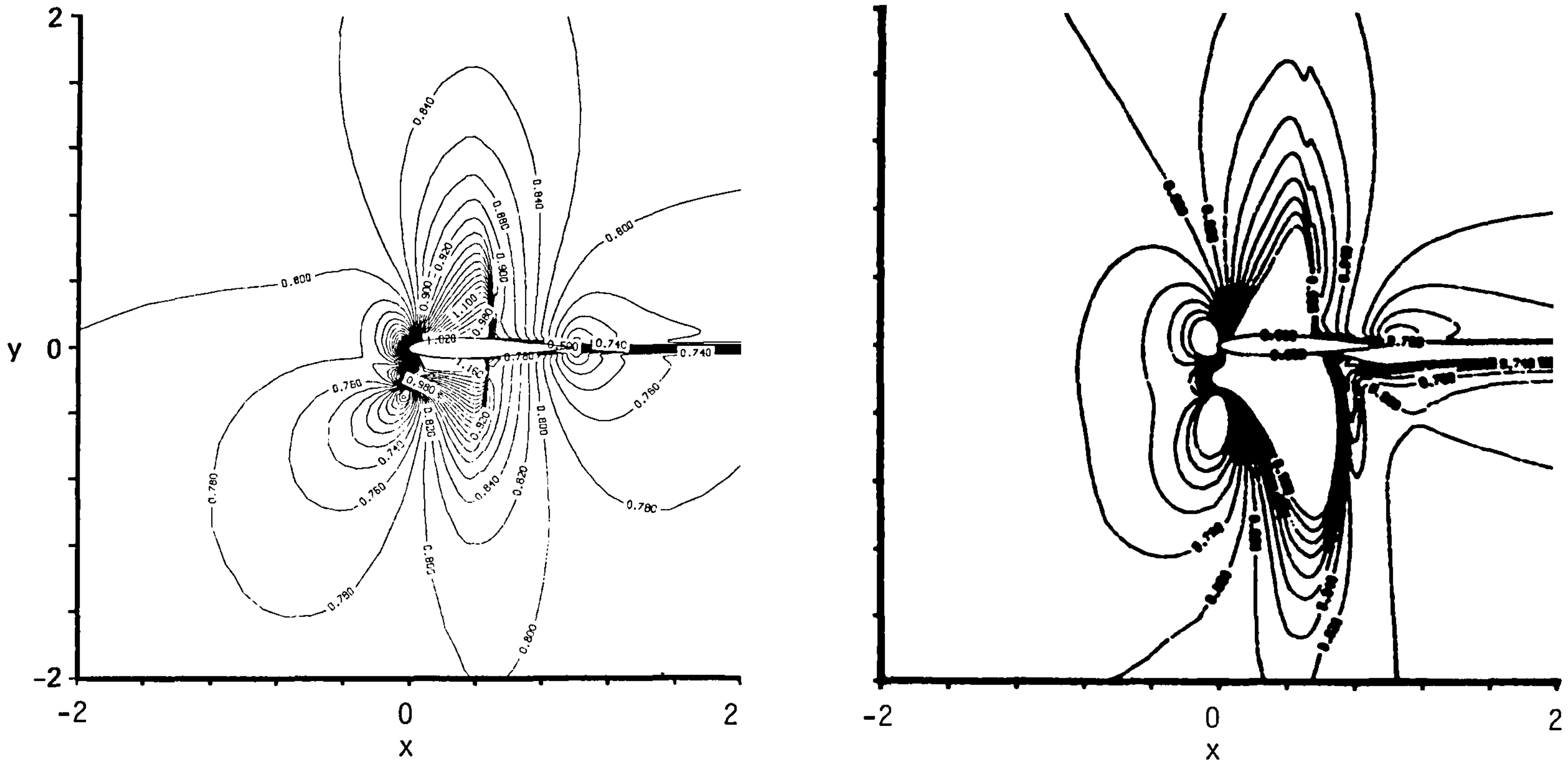

b) MACH NUMBER CONTOURS

Figure 13 continued.

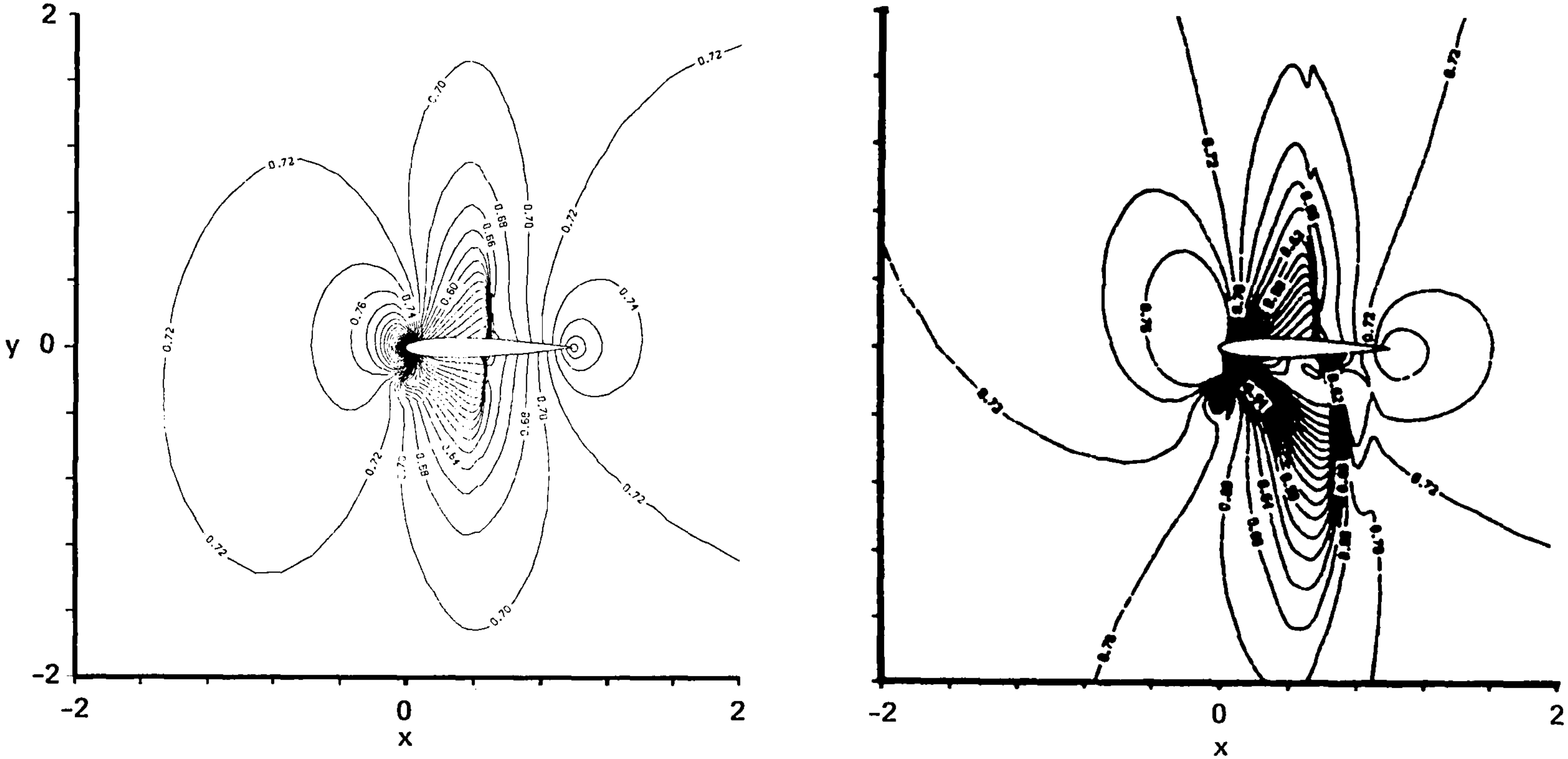

c) PRESSURE CONTOURS

Figure 13 concluded.

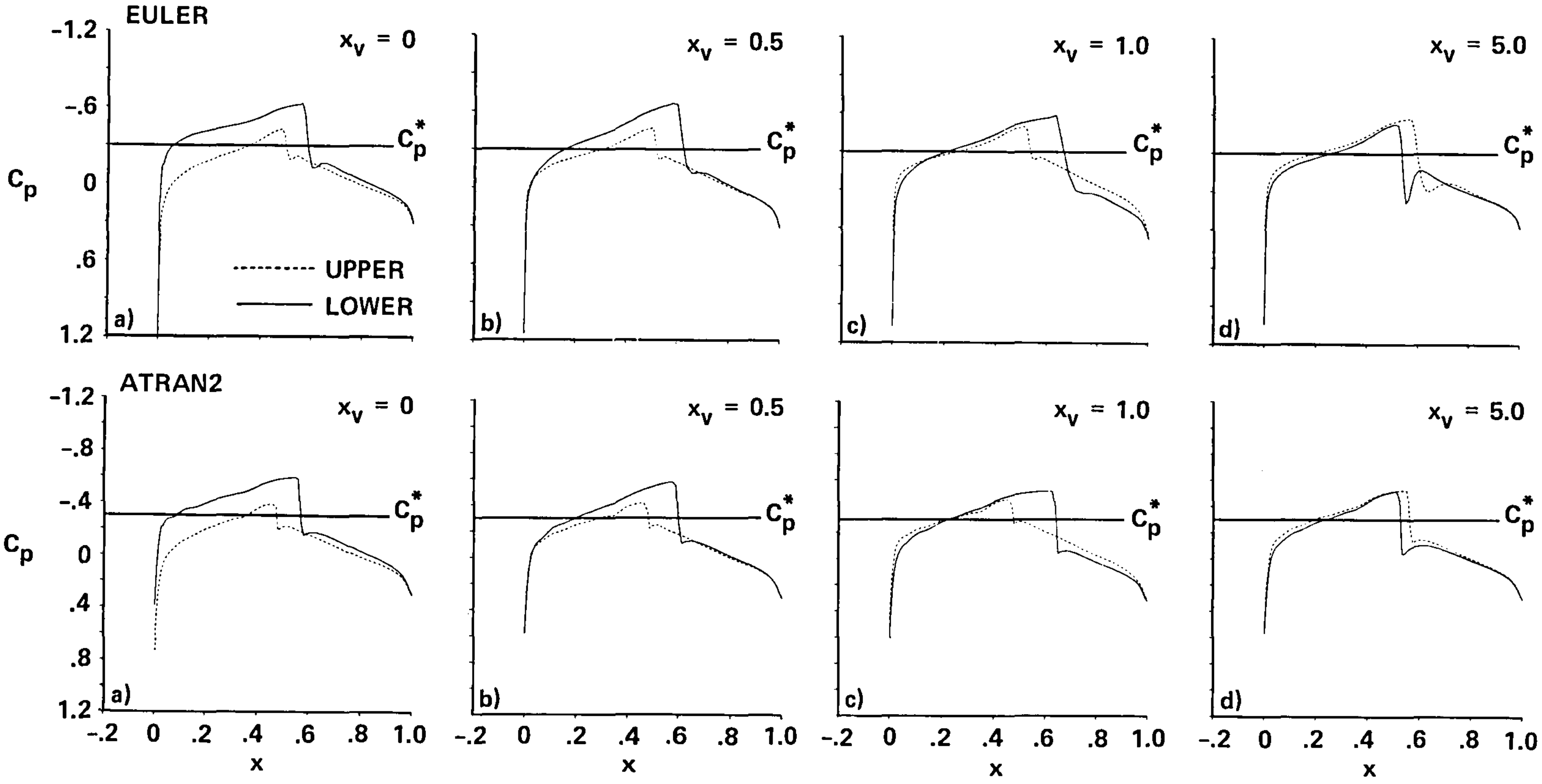

Figure 14 . Instantaneous pressure distributions during an airfoil-vortex unsteady interaction: Euler and ATRAN2 solutions, NACA 64A006 airfoil, $M_\infty = 0.85$, $\alpha = 0$ deg., $\Gamma = 0.2$, $x_o = -9.5$, $y_o = y_v = -0.52$.

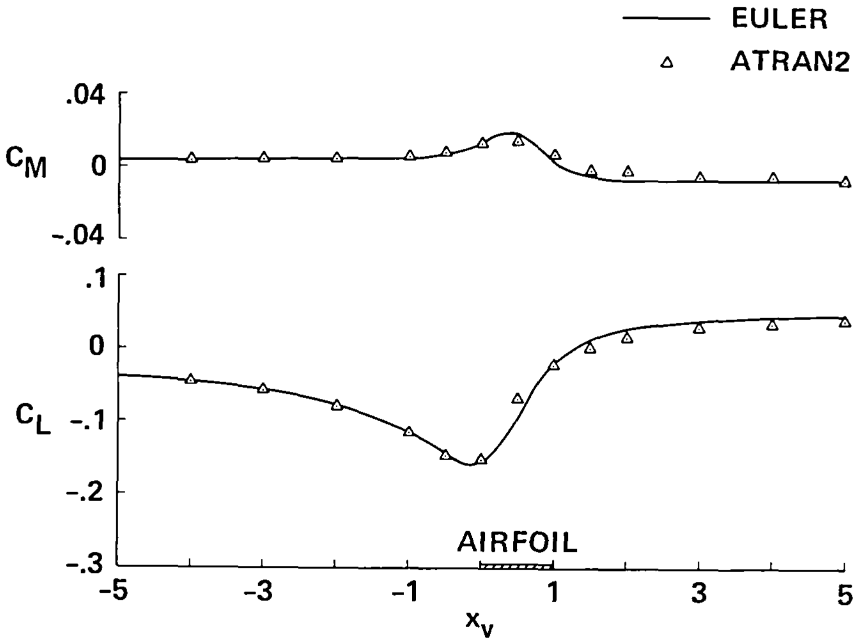

Figure 15. Lift and pitching-moment variations with instantaneous x-position of the vortex for the conditions of Fig. 14 .

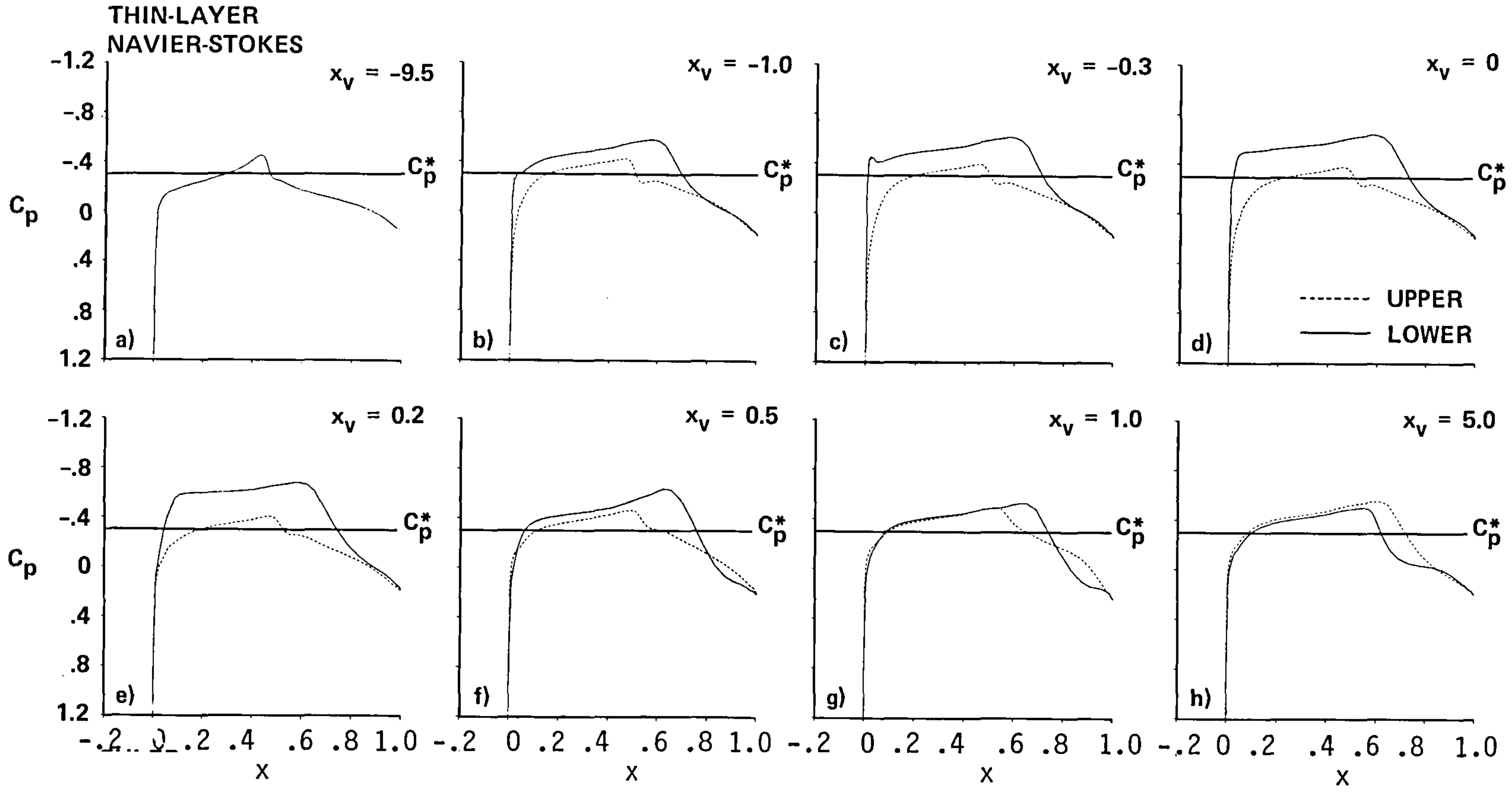

Figure 16a . Instantaneous pressure distributions during an airfoil-vortex unsteady interaction: Thin-layer Navier-Stokes solution, NACA 64A006 airfoil, $M_\infty = 0.85$, $\alpha = 0$ deg., $\Gamma = 0.2$, $y_v = -0.26$.

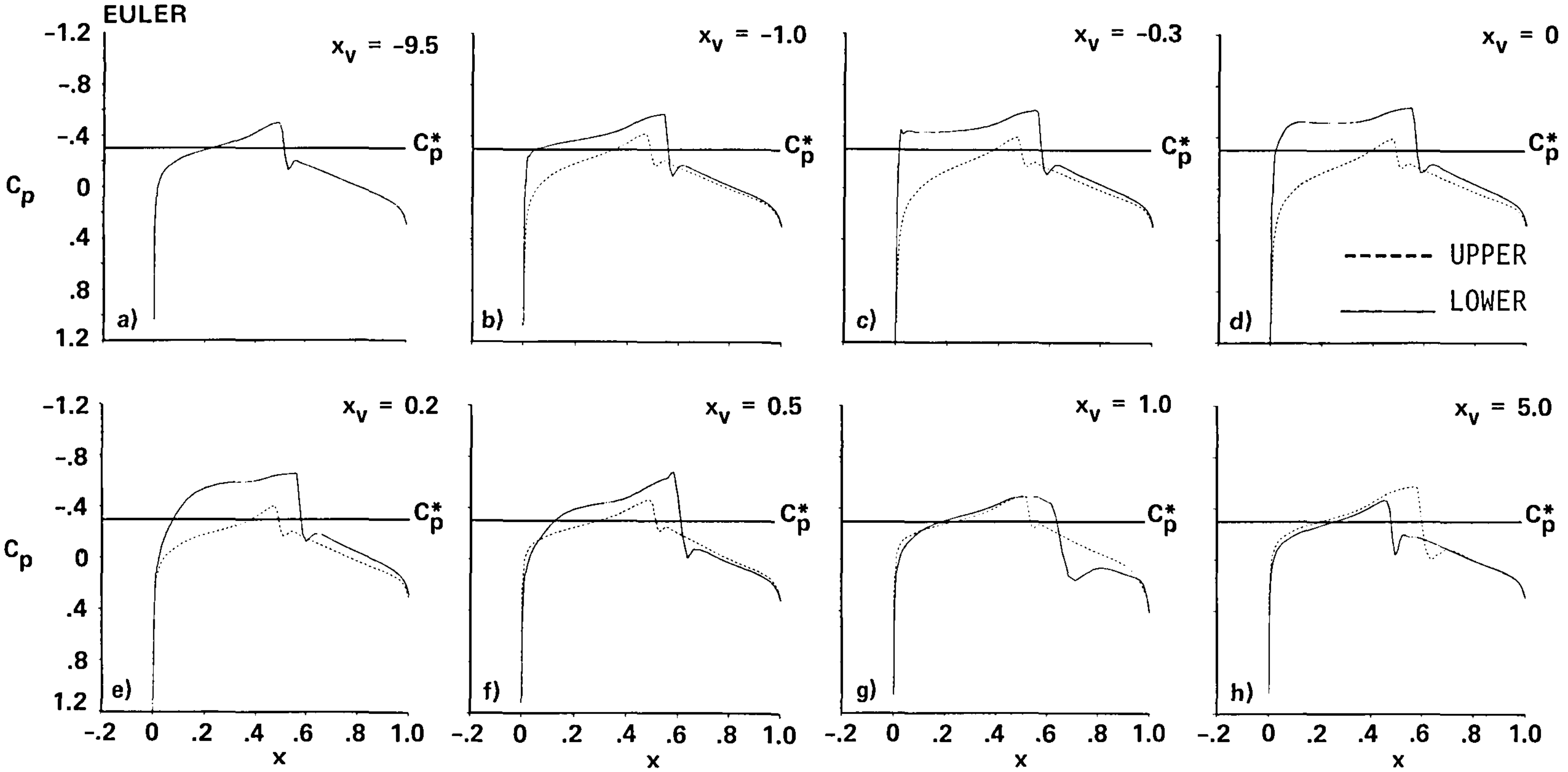

Figure 16b. Instantaneous pressure distributions during an airfoil-vortex unsteady interaction: Euler solution, NACA 64A006 airfoil, $M_\infty = 0.85$, $\alpha = 0$ deg., $\Gamma = 0.2$, $y_v = -0.26$.

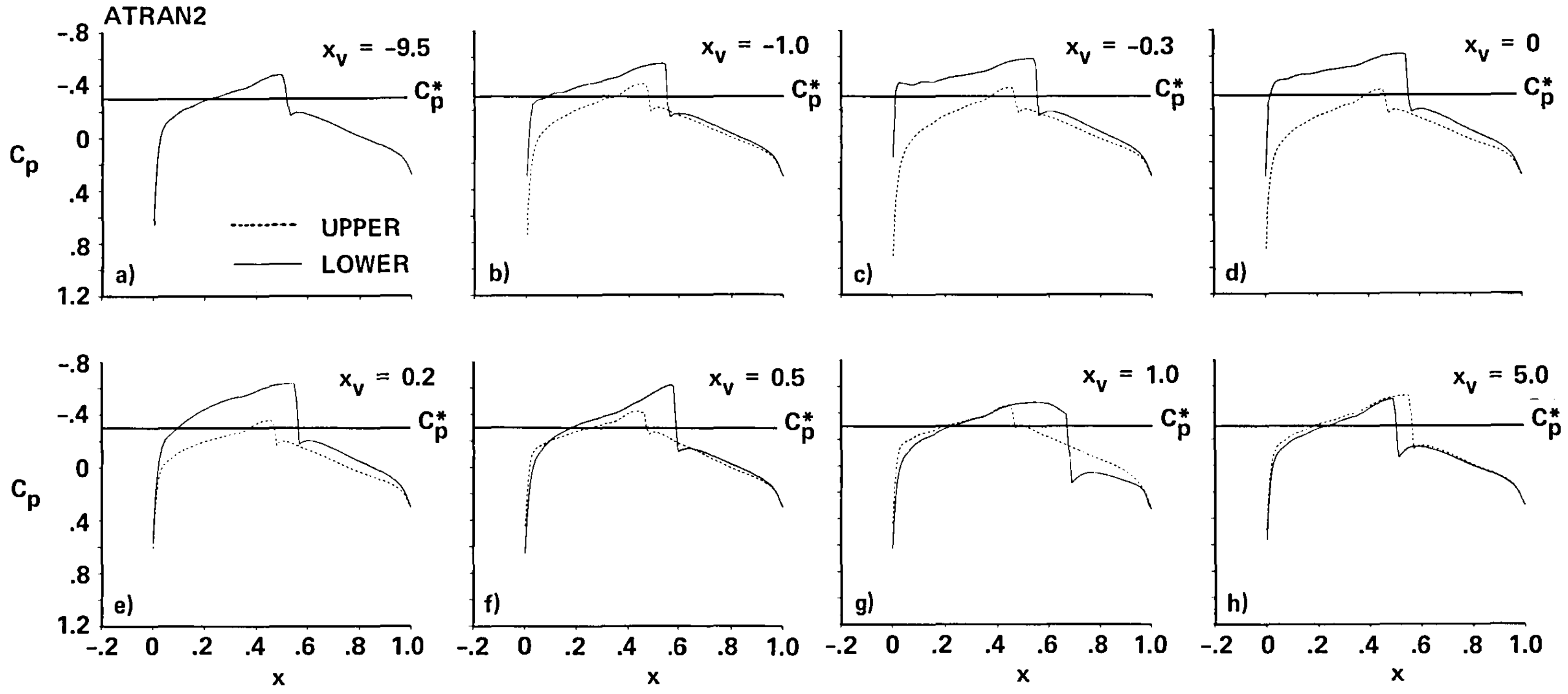

Figure 16c. Instantaneous pressure distributions during an airfoil-vortex unsteady interaction: ATRAN2 solution, NACA 64A006 airfoil, M_∞ = 0.85, α = 0 deg., Γ = 0.2, y_v = -0.26.

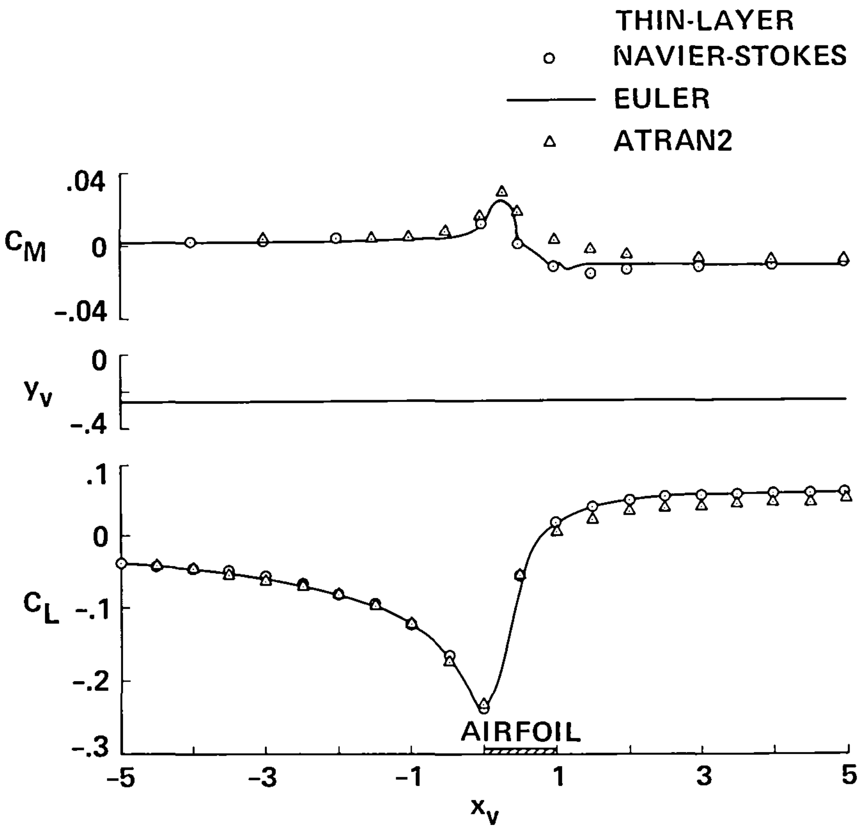

Figure 17. Lift and pitching-moment variations with instantaneous x-position of the vortex for the conditions of Figure 16.

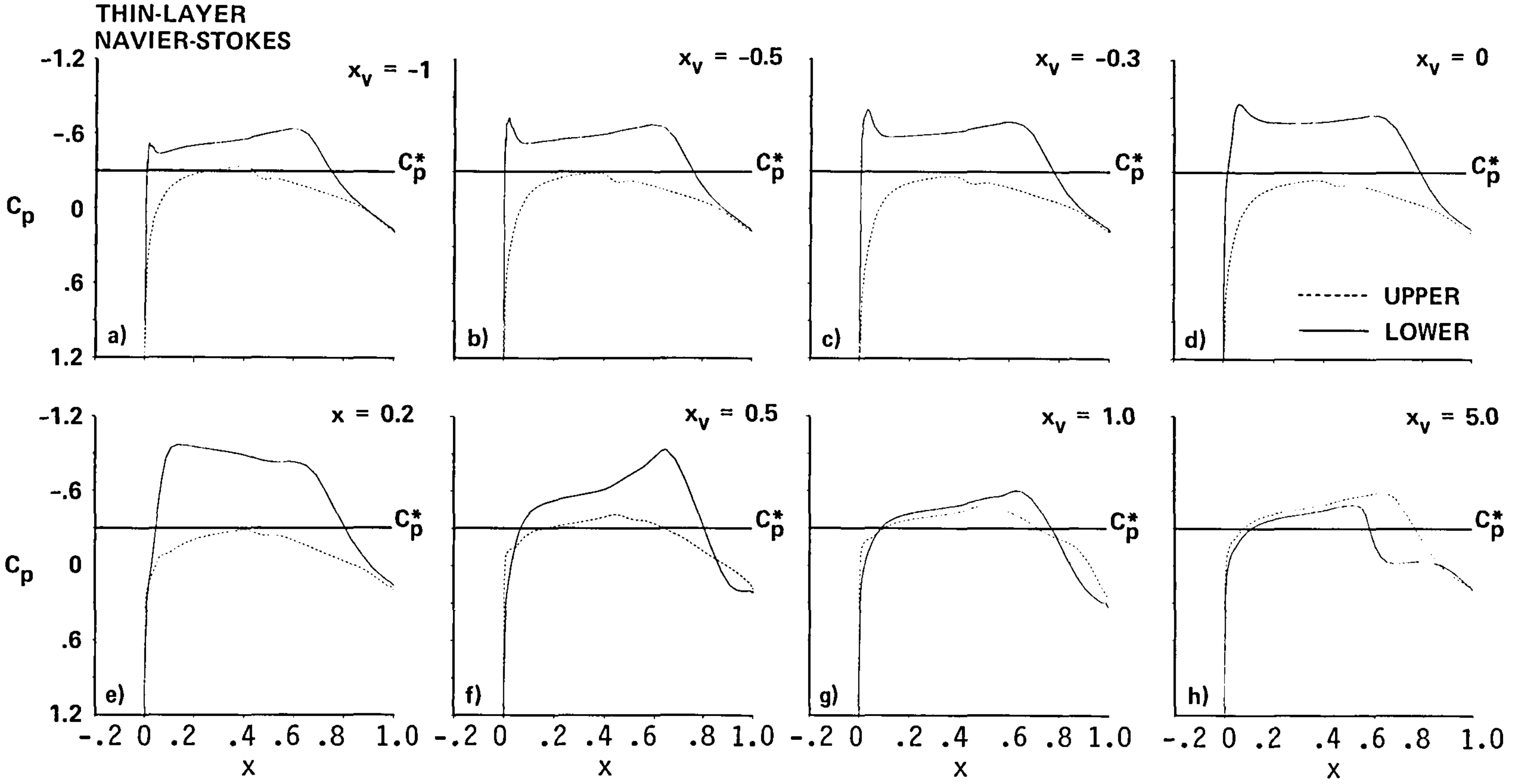

Figure 18a. Instantaneous pressure distributions during an airfoil-vortex, unsteady interaction: Thin-layer Navier-Stokes solution, NACA 64A006 airfoil, $M_\infty = 0.85$, $\alpha = 0$ deg., $\Gamma = 0.4$, $y_v = -0.26$.

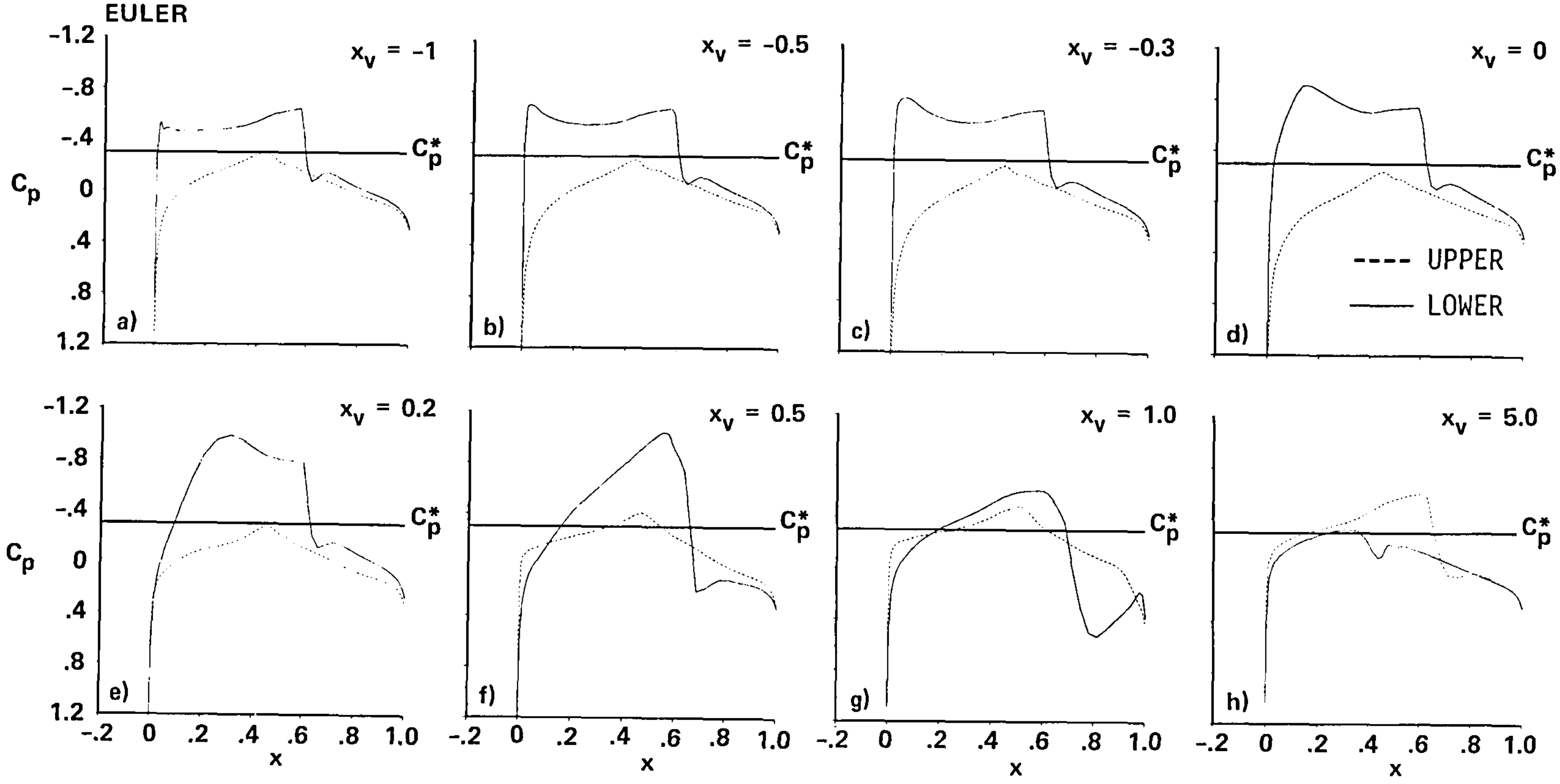

Figure 18b . Instantaneous pressure distributions during an airfoil-vortex unsteady interaction: Euler solution, NACA 64A006 airfoil, $M_\infty = 0.85$, $\alpha = 0$ deg., $\Gamma = 0.4$, $y_v = -0.26$.

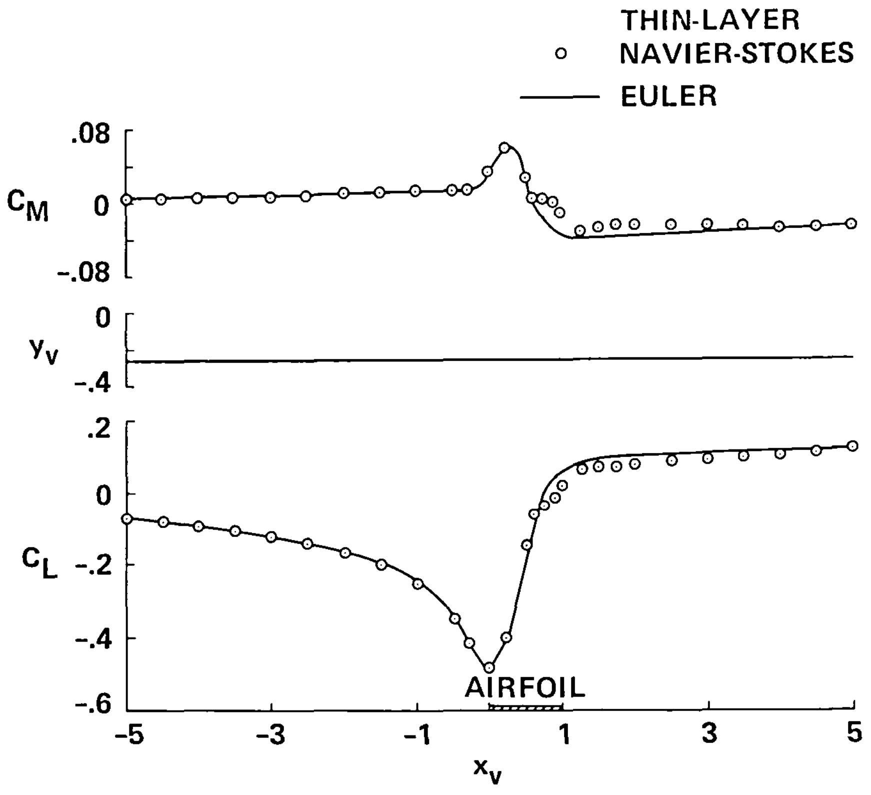

Figure 19. Lift and pitching-moment variations with instantaneous x-position of the vortex for the conditions of Figure 18.

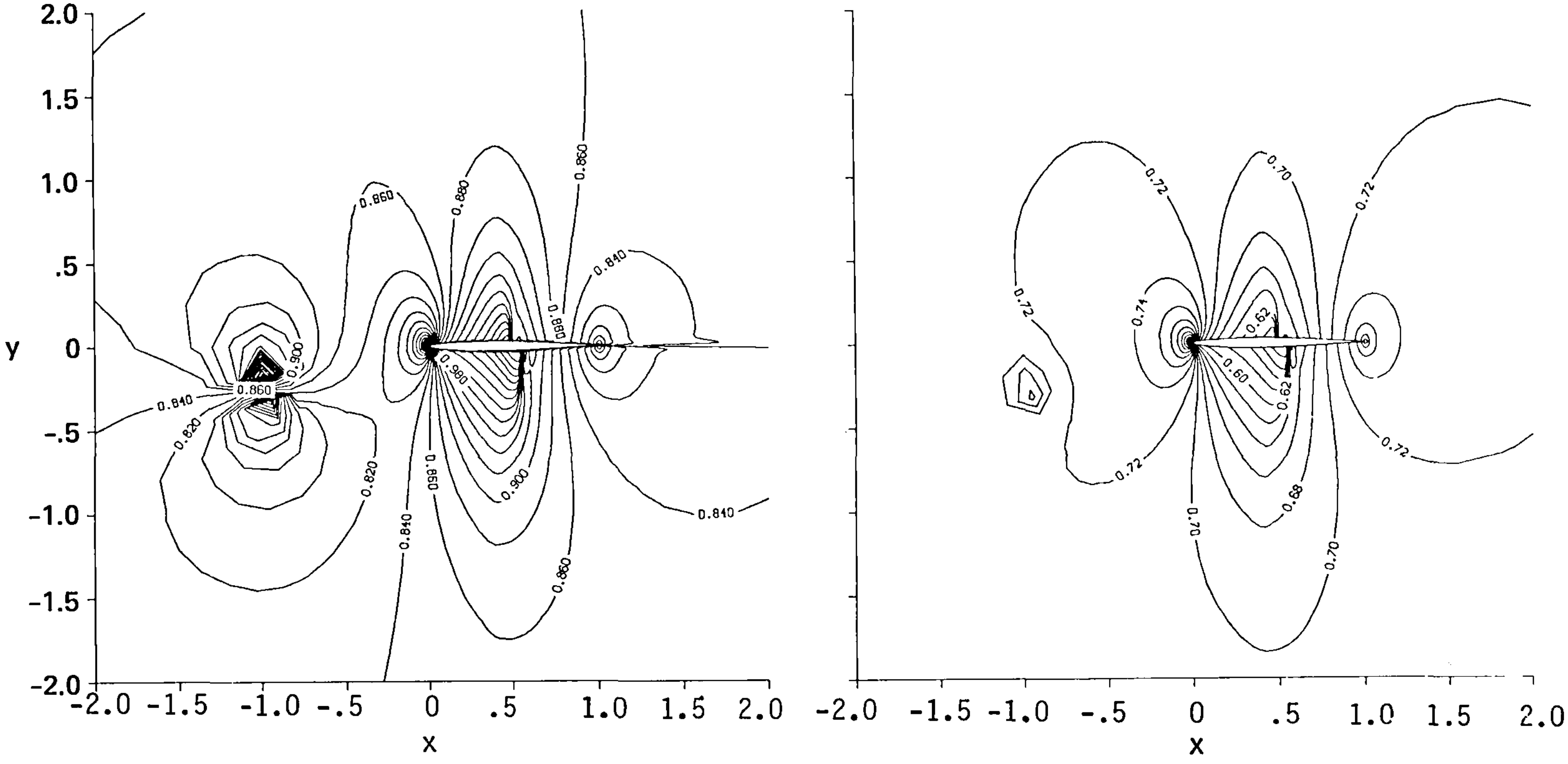

a) MACH CONTOURS

b) PRESSURE CONTOURS

Figure 20 . Euler results of the flowfield Mach number and pressure contours during an airfoil-vortex unsteady interaction: NACA 64A006 airfoil, $M_\infty = 0.85$, $\alpha = 0$ deg., $\Gamma = 0.2$, $x_v = -1$, $y_v = -0.26$.

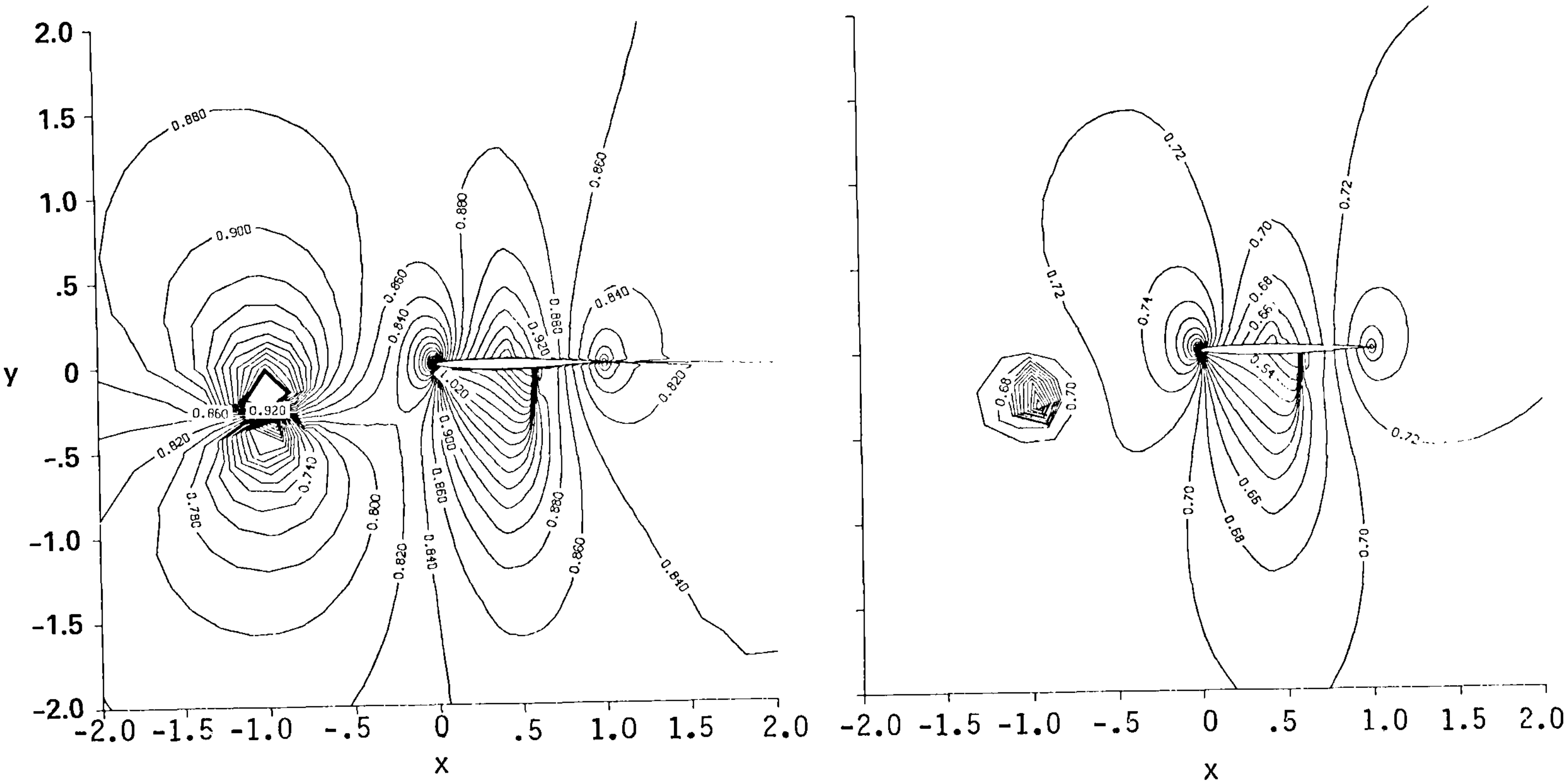

a) MACH CONTOURS

b) PRESSURE CONTOURS

Figure 21. Euler results of the flowfield Mach number and pressure contours during an airfoil-vortex unsteady interaction: NACA 64A006 Airfoil, $M_\infty = 0.85$, $\alpha = \upsilon$ deg., $\Gamma = 0.4$, $x_v = -1$, $y_v = -0.26$.

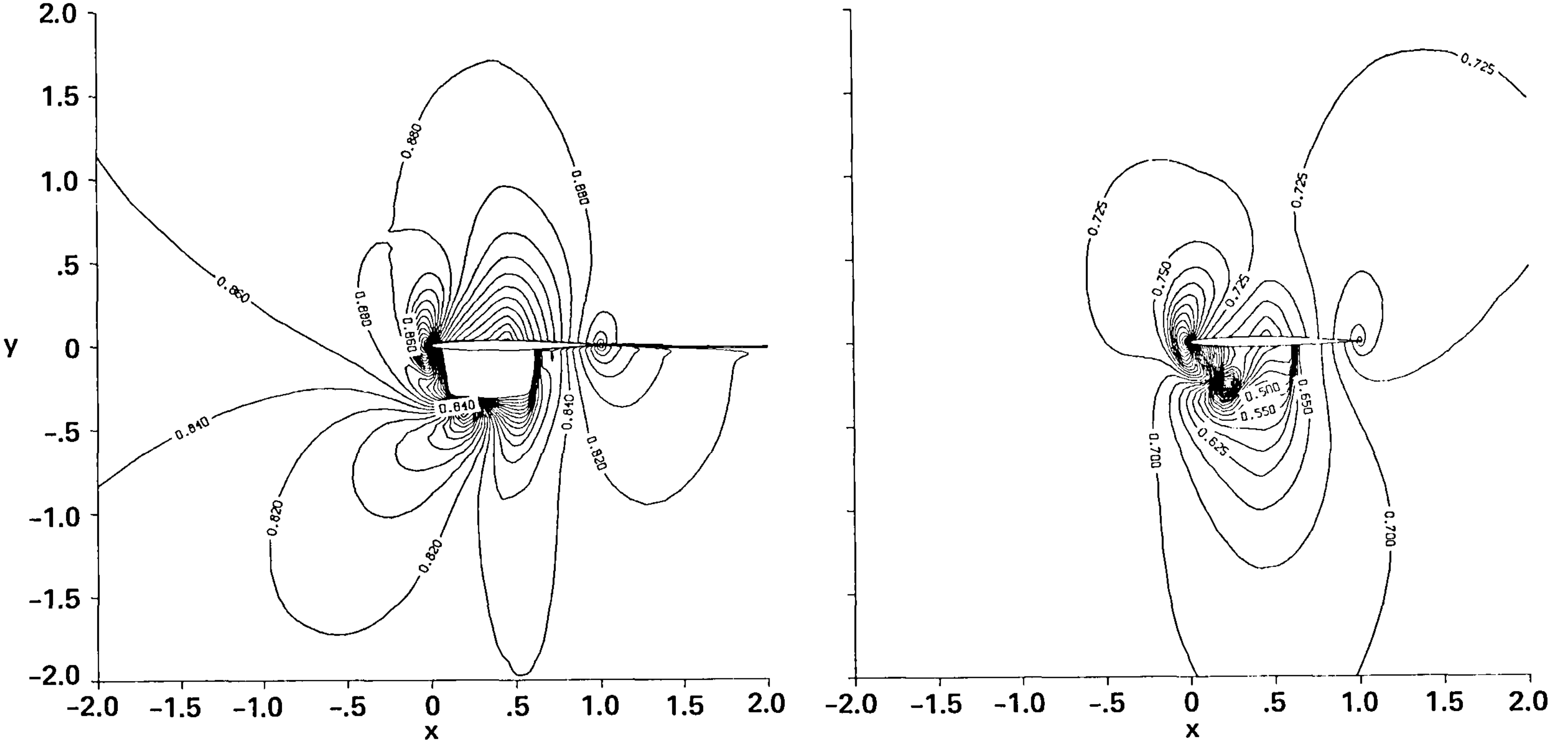

a) MACH CONTOURS

b) PRESSURE CONTOURS

Figure 22. Euler results of the flowfield Mach number and pressure contours during an airfoil-vortex unsteady interaction: NACA 64A006 airfoil, $M_\infty = 0.85$, $\alpha = 0$ deg., $\Gamma = 0.4$, $x_v = 0.2$, $y_v = -0.26$.

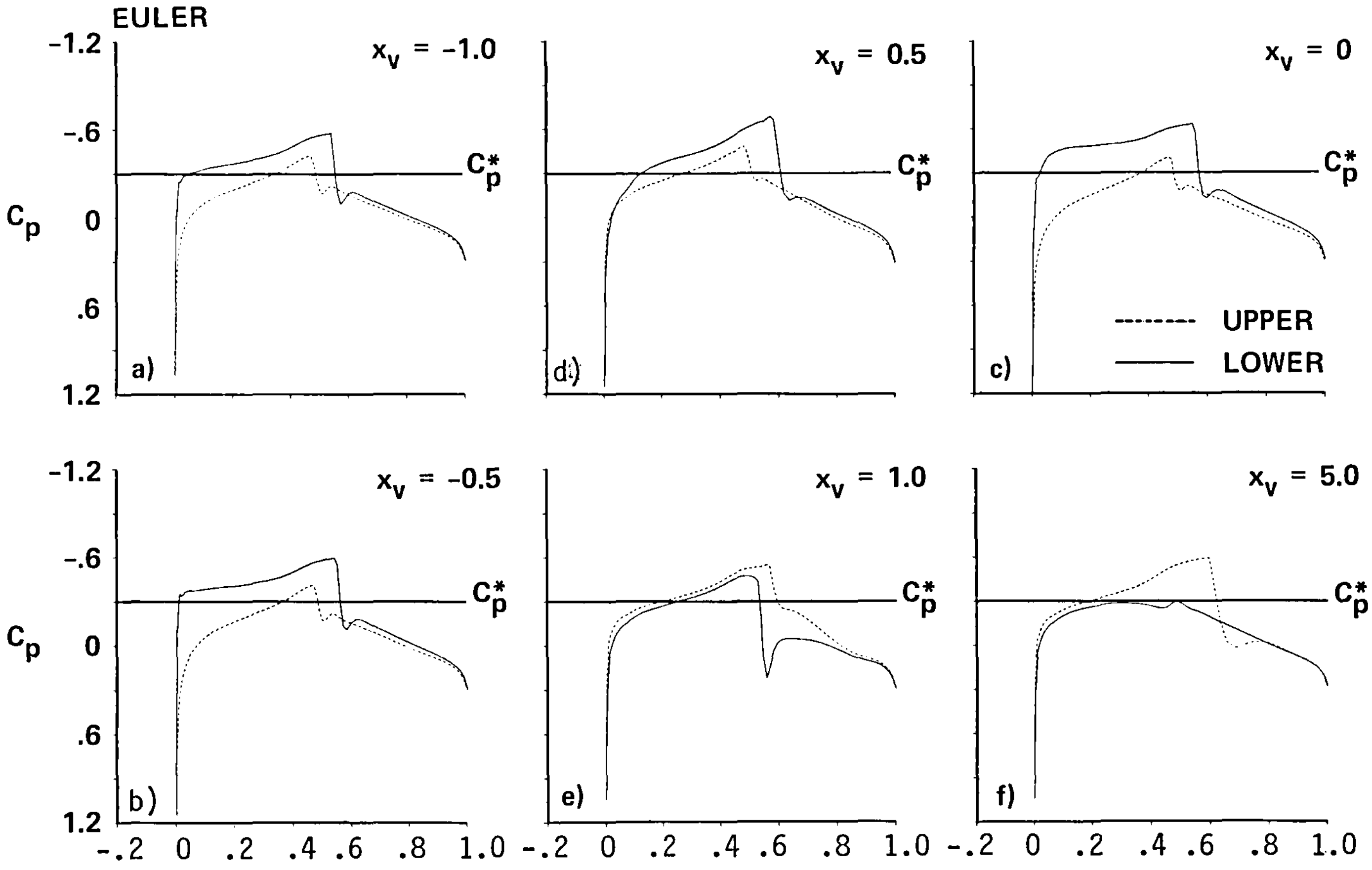

Figure 23a. Instantaneous pressue distributions during an airfoil-vortex unsteady interaction: Euler solution, NACA 64A006 airfoil, $M_\infty = 0.85$, $\alpha = 0$ deg., $\Gamma = 0.2$, $x_0 = -9.5$, $y_0 = -0.26$. Vortex is moving in a force free path.

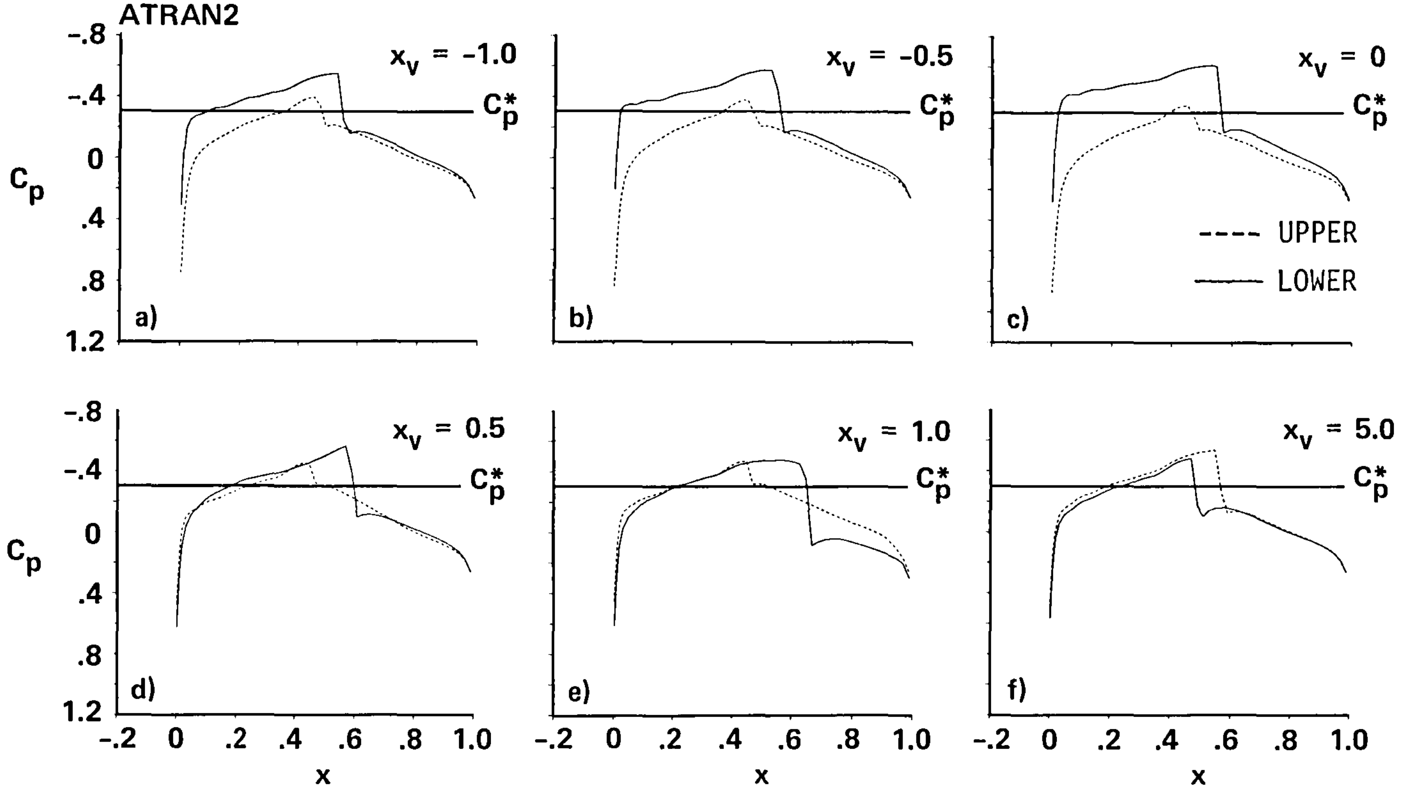

Figure 23b. Instantaneous pressure distributions during an airfoil-vortex unsteady interaction: ATRAN2 solution, NACA 64A006 airfoil, $M_\infty = 0.85$, $\alpha = 0$ deg., $\Gamma = 0.2$, $x_0 = -9.5$, $y_0 = -0.26$. Vortex is moving in a force free path.

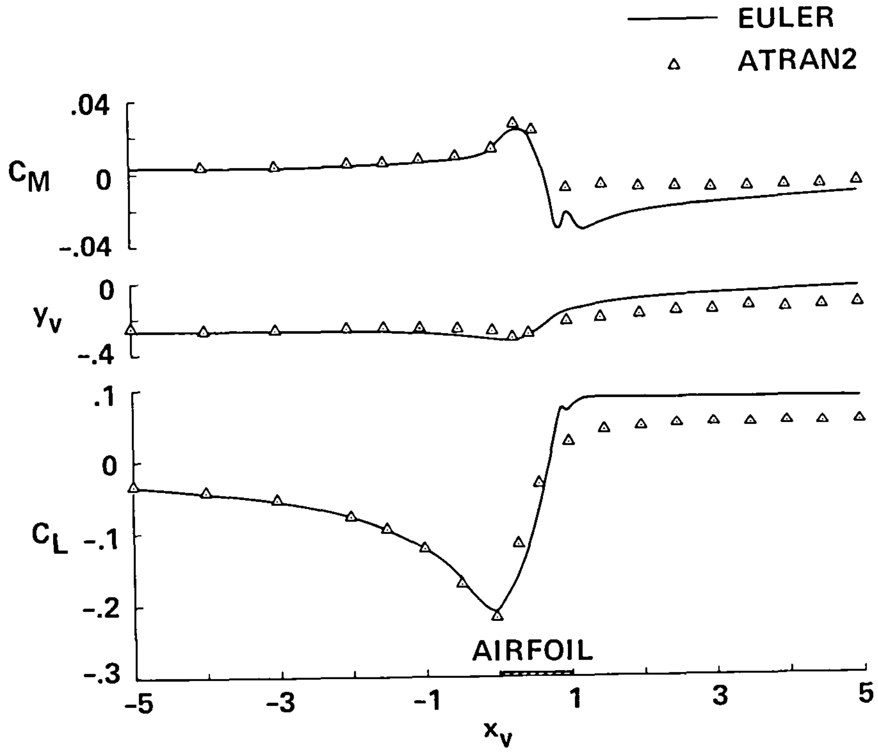

Figure 24. Lift and pitching-moment variations with instantaneous x-position of the force free vortex for the conditions of Figure 23.

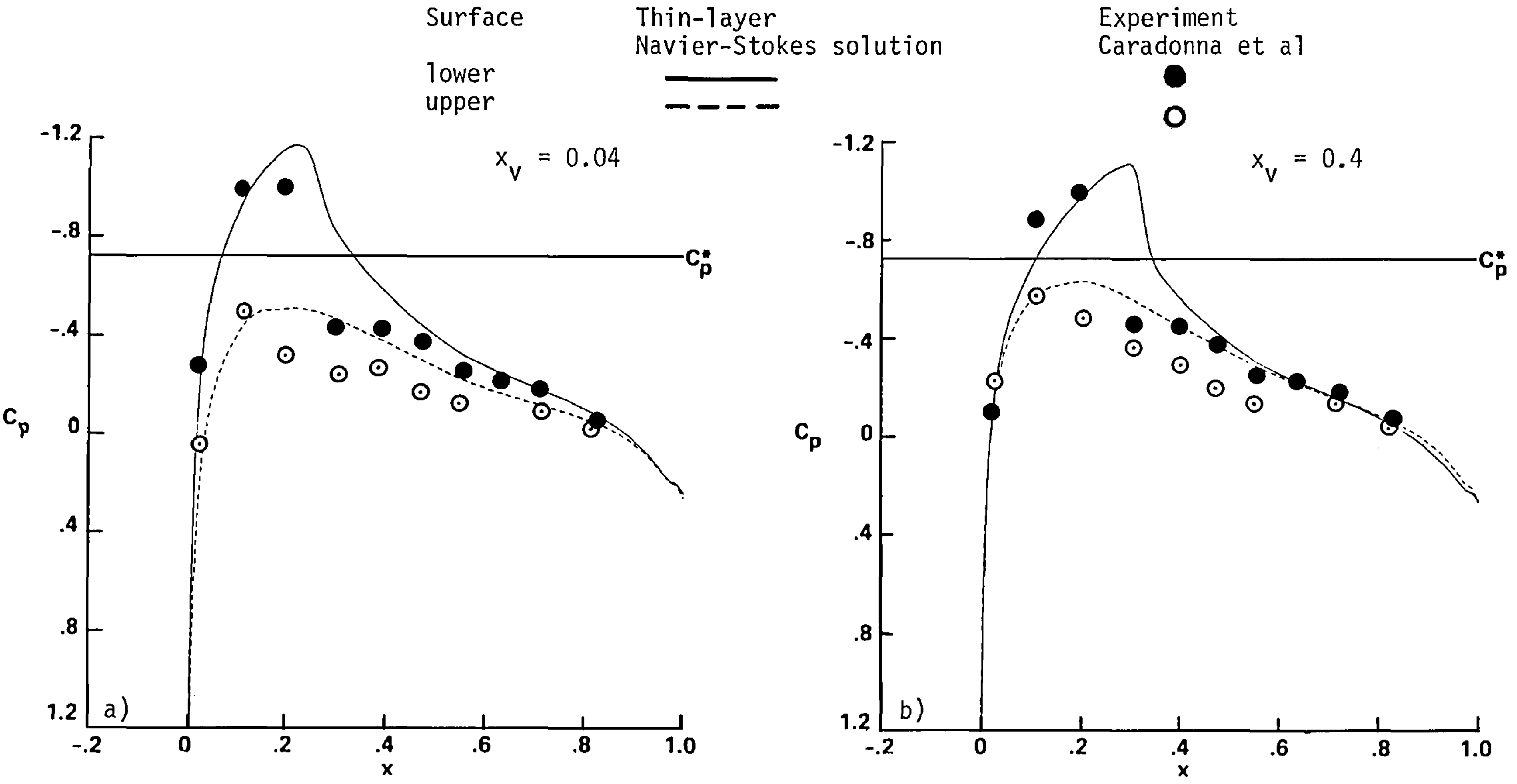

Figure 25 . Instantaneous chordwise pressure distribution as a function of the vortex position. Thin-layer Navier-Stokes solution: NACA 0012 airfoil, $M_\infty = 0.714$, $\alpha = 0$ deg., vortex strength $\Gamma = 0.31$, and $y_o = -0.4$. Vortex is convecting in a force free path.

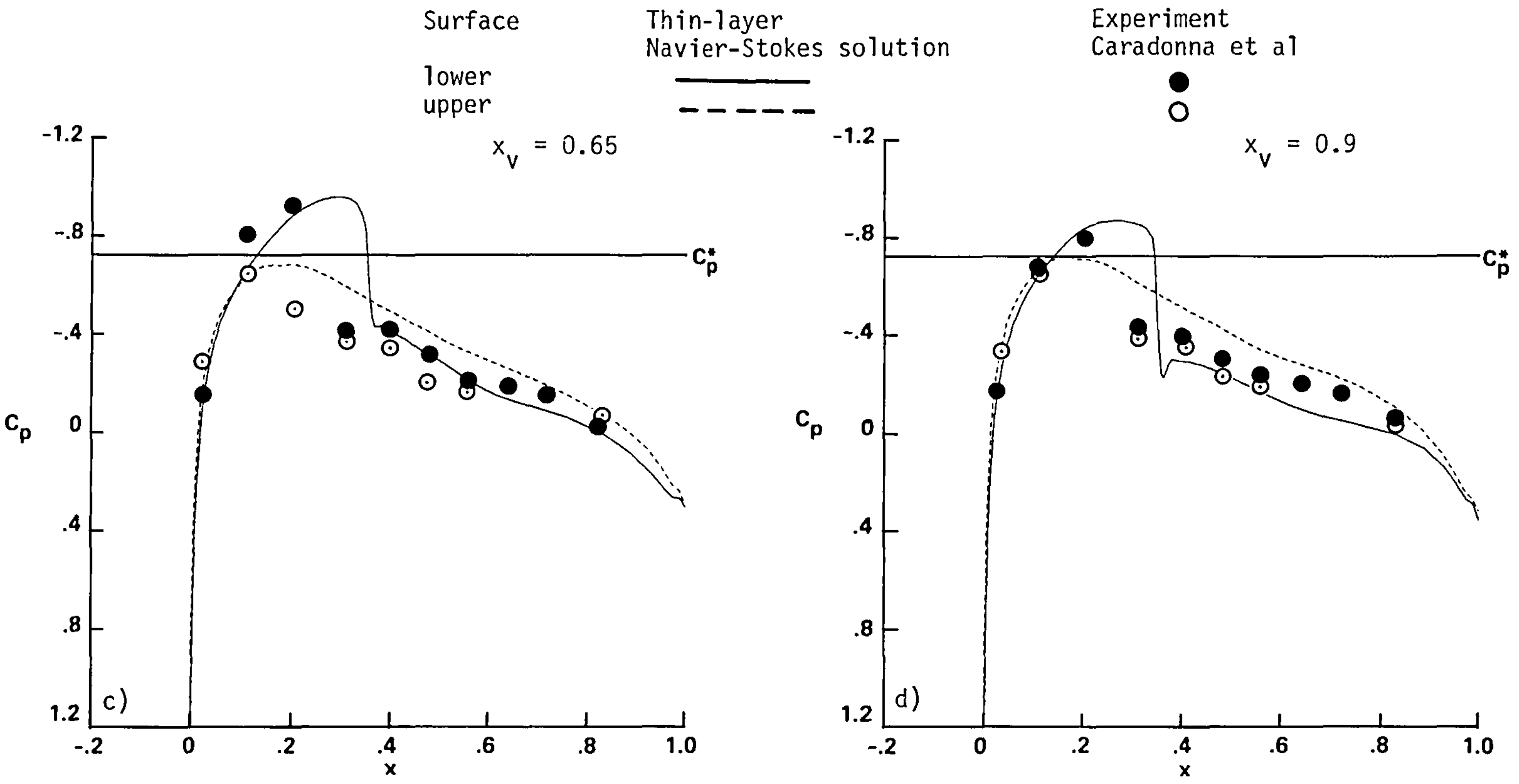

Figure 26 . Instantaneous chordwise pressure distribution as a function of the vortex position. Thin-layer Navier-Stokes solution: NACA 0012 airfoil, M_∞ = 0.714, α = 0 deg., vortex strength Γ = 0.31, and y_0 = -0.4. Vortex is convecting in a force free path.

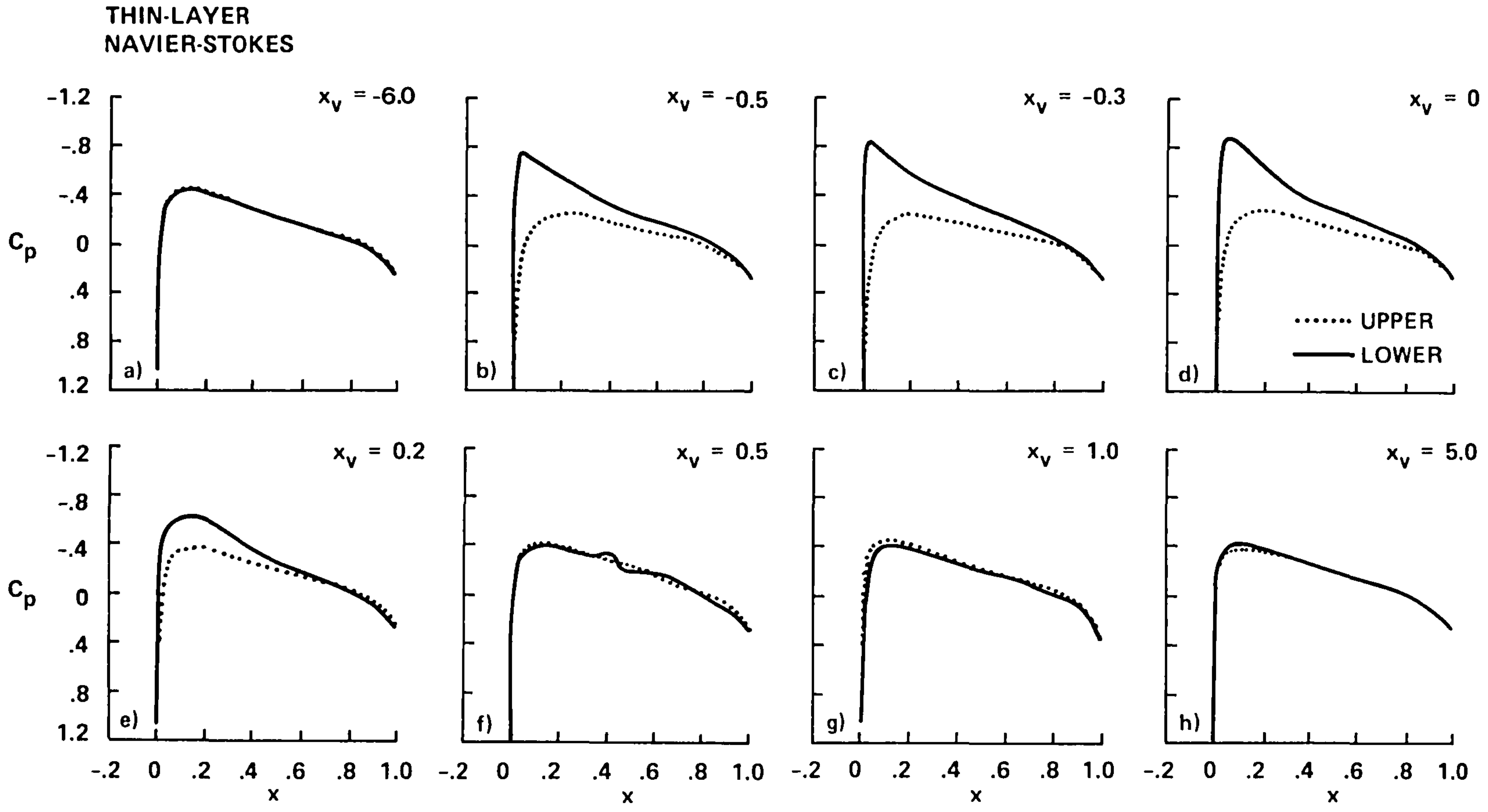

Figure 27a. Instantaneous pressure distributions during an airfoil-vortex unsteady interaction: Thin-layer Navier-Stokes solution, NACA 0012 airfoil, $M_\infty = 0.3$, $\alpha = 0$ deg., $\Gamma = 0.2$, $y_o = y_v = -0.26$.

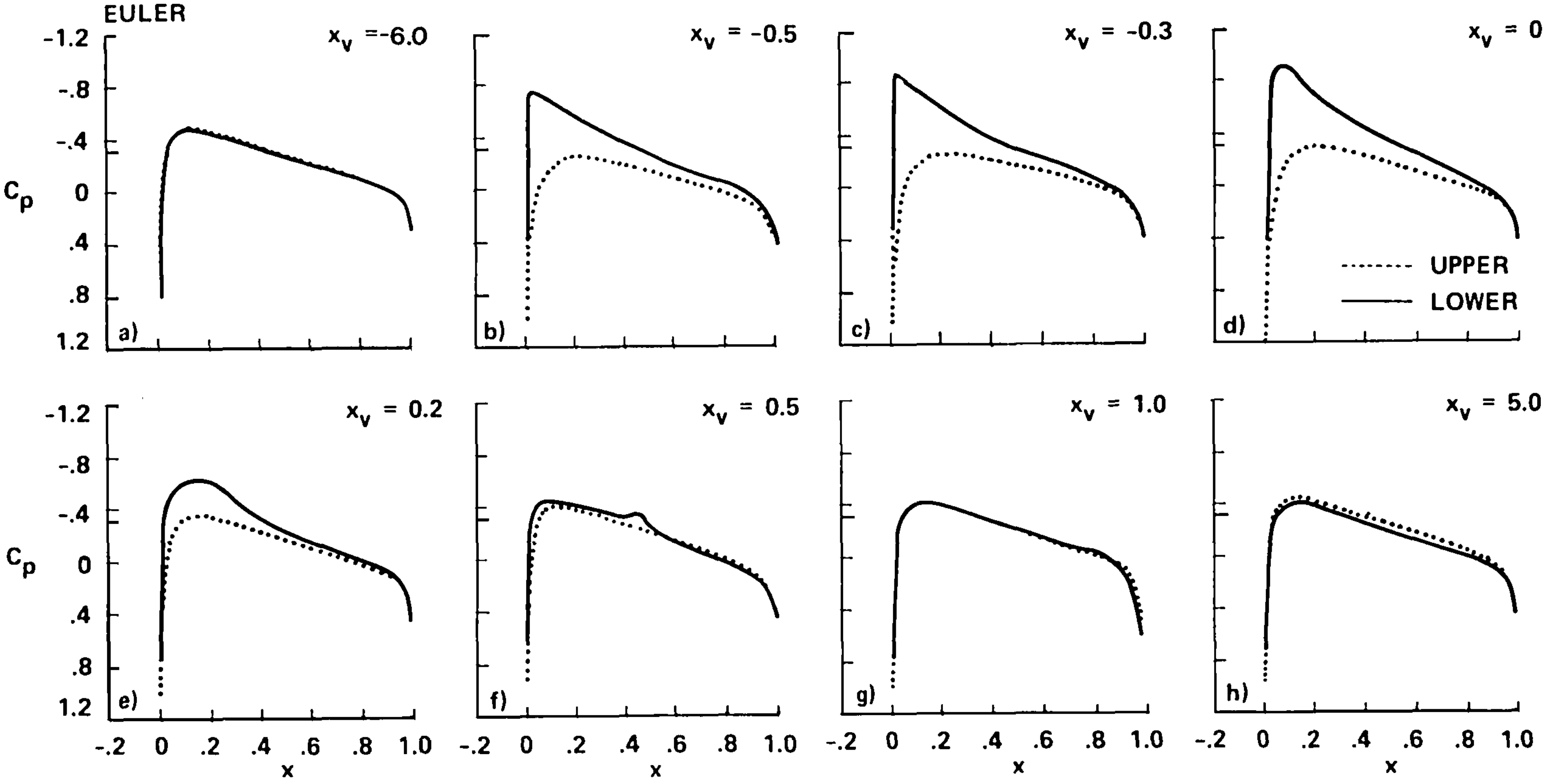

Figure 27b. Instantaneous pressure distributions during an airfoil-vortex unsteady interaction: Euler solution, NACA 0012 airfoil, $M_\infty = 0.30$, $\alpha = 0$ deg., $\Gamma = 0.2$, $y_0 = y_v = -0.26$.

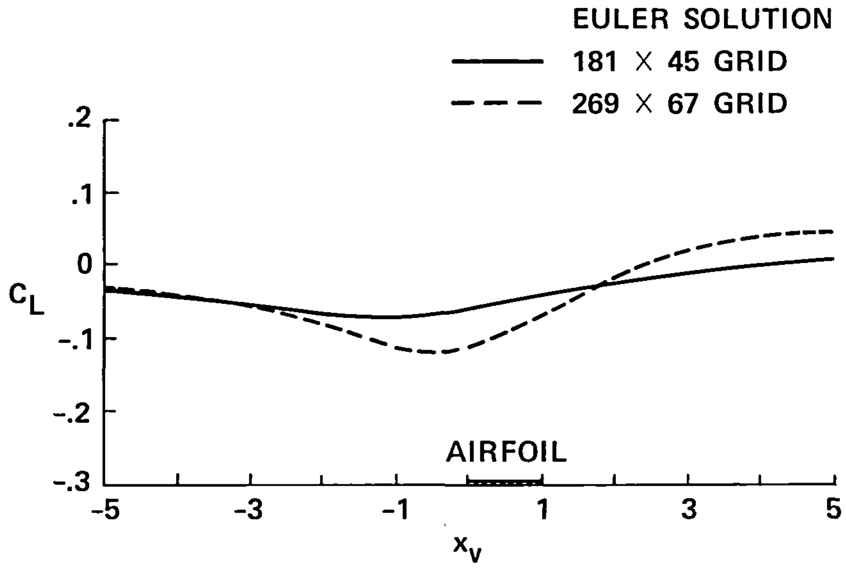

Figure 28. Lift coefficient variation with instantaneous x-location of the vortex for two grids using non-perturbation approach: Euler solution, NACA 64A006 airfoil, $M_\infty = 0.85$, $\alpha = 0$ deg., $\Gamma = 0.2$, and $y_0 = -0.26$.

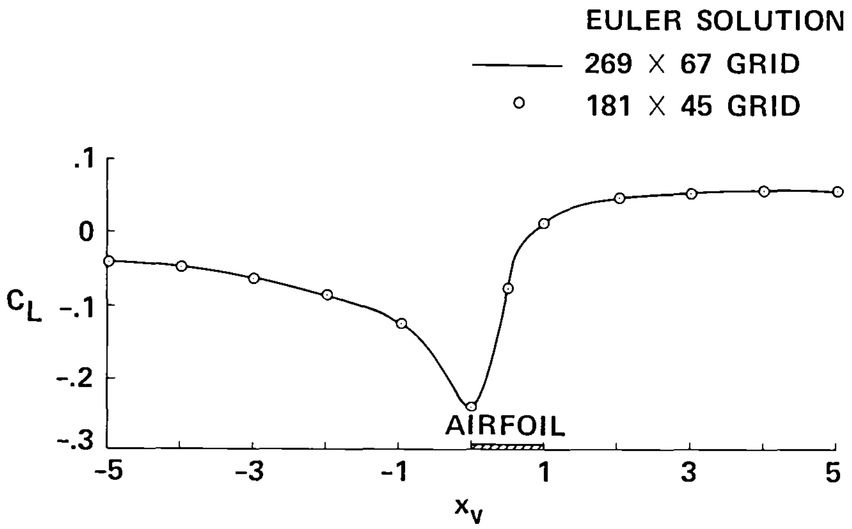

Figure 29. Lift coefficient variation with instantaneous x-location of the vortex for fine and coarse grids: Euler solution, NACA 64A006 airfoil, $M_\infty = 0.35$, $\alpha = 0$ deg., $\Gamma = 0.2$, and $y_0 = -0.26$.

1. Report No. NASA CR-3885	2. Government Accession No.	3. Recipient's Catalog No.
4. Title and Subtitle Computations of Two-Dimensional Airfoil-Vortex Interactions		5. Report Date May 1985 6. Performing Organization Code
7. Author(s) Ganapathi R. Srinivasan		8. Performing Organization Report No. FSI Report No. 84-01
9. Performing Organization Name and Address Flow Simulations, Inc. 292 Gibraltar Dr., Suite A-4 Sunnyvale, CA 94089		10. Work Unit No. T-64-57 11. Contract or Grant No. NAS2-11331 13. Type of Report and Period Covered
12. Sponsoring Agency Name and Address U.S. Army Aeromechanics Laboratory and NASA Ames Research Center Moffett Field, CA 94035		Contractor Report 14. Sponsoring Agency Code 505-31-01-01-00-21

15. Supplementary Notes

Point of Contact: Dr. W.J. McCroskey, MS 202A-1, FTS 464-6428, 415-694-6428
U.S. Army Aeromechanics Laboratory, NASA-Ames Research Center
Moffett Field, Ca 94035

16. Abstract

A numerical solution procedure to calculate the interaction of a vortex with a two-dimensional airfoil in a uniform free stream is presented along with results for several test cases. A Lamb-like analytical vortex having a finite core and convect in a uniform free stream interacts with the flowfield of NACA 0012 or NACA 64A006 airfoil in transonic and subsonic flow. Euler and thin-layer Navier-Stokes solutions are computed and the results are compared with the results from transonic small disturbance code and experimental results where they are available. Most of the interactions considered in this study are strong, in the sense that the vortex produced significant and nonlinear distortions of the flowfield. For interactions within the limits of transonic small disturbance assumptions, the three methods gave qualitatively similar results of a two-bladed helicopter rotor suggest that the time-lag effects of the free stream velocity approaching the blade may be important and should be considered in the analysis. In general, the results show a tremendous influence of the interacting vortex on the flowfield around the airfoil. This is particularly true when the vortex is stationary. For a convecting vortex, the most dramatic changes in the flowfield seem to occur when the vortex is within one chord of the airfoil.

17. Key Words (Suggested by Author(s)) Compressible flow Shock wave Prescribed vortex Force-free vortex	18. Distribution Statement Unclassified - Unlimited STAR Category 02

19. Security Classif. (of this report) Unclassified	20. Security Classif. (of this page) Unclassified	21. No. of Pages 90	22. Price A05

For sale by the National Technical Information Service, Springfield, Virginia 22161

NASA-Langley, 1985

National Aeronautics and
Space Administration

Washington, D.C.
20546

Official Business
Penalty for Private Use, $300

NASA